Generating cognate epitope sequences of T-cell receptors with a generative transformer

Minuk Ma[1], Wilson Tu[1], Carlos Vasquez-Rios[1], Jiarui Ding[1*]

[1]*Department of Computer Science, University of British Columbia, Vancouver, British Columbia, Canada, V6T 1Z4*

**Corresponding author jiarui.ding@ubc.ca*

Single-cell TCR sequencing enables high-resolution analysis of T Cell Receptor (TCR) diversity and clonality, offering valuable insights into immune responses and disease mechanisms. However, identifying cognate epitopes for individual TCRs requires complex and costly functional assays. Recent deep learning models have demonstrated the ability to predict TCR-epitope binding affinities. However, direct application of these predictors in repertoire-wide analyses has been hindered by the absence of corresponding epitope information in typical single-cell TCR sequencing datasets. We address this challenge with EpiGen, a large-scale transformer that generates potential cognate epitope sequences solely from TCR sequences. To overcome the scarcity of TCR-epitope binding pairs ($\approx 100,000$), we developed a label propagation scheme that incorporates predictions of high binding affinities as pseudo-labels, effectively leveraging a vast amount of unpaired TCR and epitope sequences. Our approach involved analyzing over 70 billion potential pairs, followed by rigorous quality control to eliminate redundancy. We introduced Antigen Category Filter to ensure the pseudo-labeled dataset effectively represents a large TCR repertoire by controlling the distribution of antigen categories based on fundamental immunological principles about $CD8^+$ T cells. The epitopes generated by EpiGen were thoroughly validated for binding affinities and naturalness in multiple test settings. To demonstrate EpiGen's practical utility, we used it to analyze paired single-cell RNA and TCR sequencing data from cancer and COVID-19 patients. The analyses identified tumor-associated and COVID-19-associated $CD8^+$ T cells that expressed characteristic cytotoxic markers, which was consistent with the roles of disease-specific T cells and multiple previous studies.

Keywords: single-cell TCR-sequencing, TCR-peptide interaction, sequence-to-sequence generation, label propagation, deep learning, transformer

1 Introduction

The adaptive immune system is a specialized defense mechanism in vertebrates that provides long-lasting protection against pathogens by recognizing and memorizing specific antigens. T cells play a vital role in identifying and eliminating infected cells through their unique T cell receptors (TCRs). $CD8^+$ T cells, in particular, inspect endogenous peptides displayed on class I Major Histocompatibility Complex (MHC) molecules, expressed ubiquitously across human cells[1]. Upon recognition of abnormal peptides, such as those of viral or tumoral origin, cytotoxic $CD8^+$ T cells can initiate apoptosis in the target cell, given appropriate co-stimulatory signals[2]. The specific antigen fragment recognized by the immune system is termed an epitope. For T cells, epitopes are peptide fragments presented on MHC molecules, serving as key targets for TCR recognition. The Complementarity Determining Region 3 (CDR3) of the TCR is primarily responsible for epitope binding, with the interaction affinity determined by the physicochemical properties of both protein sequences. The extreme polymorphism of CDR3, resulting from VDJ recombination[3,4], enables a diverse range of immune responses but presents challenges for quantitative modeling due to the vast sequence diversity at the TCR-pMHC (peptide-loaded MHC) interface.

Prior works in computational TCR analysis can be broadly categorized into three approaches: diversity metrics for TCR repertoire analysis, TCR clustering methods, and TCR-pMHC binding affinity prediction models. To quantify the focused nature of immune responses, various TCR diversity metrics have been proposed, including Shannon entropy[5], Simpson index[6], and Rényi diversity[7]. Janarthanam et al[8]. employs D50, the minimum number of unique clonotypes constituting 50% of the total, to track clonality changes in pediatric eosinophilic esophagitis patients during dietary interventions. TCRDivER[9] introduces a similarity-sensitive diversity measure that jointly considers clone size and sequence similarity. While these diversity metrics effectively capture T cell clonal expansion patterns, they provide limited insight into antigen specificity. Analysis of TCR repertoire data has been facilitated by various TCR clustering methods[10–13]. These methods aim to group TCRs with potentially similar antigen specificity. GLIPH2[10] uses a statistical method to identify TCR motifs that are overrepresented in query sets compared to background TCR repertoires. DeepTCR[12] leverages deep learning-based autoencoders to learn latent TCR representations that facilitate clustering of similar sequences. However, these clustering approaches, while valuable for repertoire analysis and motif discovery, face two key limitations. First, TCRs within the same cluster may not share antigen specificity. Second, the methods cannot directly predict the cognate epitopes for the identified TCR clusters. Recent advances in machine learning have enabled direct prediction of TCR-pMHC binding affinity[14–26]. Models such as pMTnet[14] address data scarcity through transfer learning, while PanPep[15] employs model-agnostic meta-learning to enhance generalization to unseen data. However, these binding affinity prediction models have limited utility in analyzing TCR repertoires, as repertoire data typically lack corresponding epitope information, creating a barrier to functional analysis.

To address these challenges, we explore the generative modeling of epitope sequences,

inspired by the success of large-scale transformers in open-ended text generation[27–29]. By developing an efficient algorithm to identify cognate epitopes of TCRs, we aim to bridge the gap between TCR repertoire data and functional analysis. This approach can provide valuable insights for advancing personalized medicine and enhancing patient outcomes. For example, identifying tumor-specific TCRs can improve the precision of cancer therapies, allowing better targeting of cancer cells while minimizing harm to healthy tissues[30]. Furthermore, accurately identifying TCRs that respond to viral epitopes from a patient can help design more effective, customized vaccines[31].

We introduce EpiGen, a large-scale transformer model designed to generate cognate epitope sequences directly from TCR sequences. Initial experiments reveal that training transformer models solely on publicly available TCR-epitope pairs results in the generation of highly redundant epitopes across different TCRs, limiting their utility for repertoire-wide analysis. Existing protein language models (ProtGPT2[32] and ProGen2[33]), which are unconditional models optimized for long protein sequences, proved inadequate for T cell epitope generation. To overcome these limitations, we developed a semi-supervised learning approach based on label propagation[34]. This strategy leverages the vast amount of unpaired TCR and epitope sequences available from high-throughput sequencing experiments. The label propagation algorithm inspects more than 70 billion TCR-epitope pairs and harvests the ones with high binding affinity with high confidence. We further introduce the Redundancy Filter, which ensures epitope diversity in the pseudo-labeled dataset. A key innovation in our approach is the Antigen Category Filter (ACF), which calibrates the distribution of antigen categories in our training set based on established immunological principles about $CD8^+$ T cells. These distributional constraints are essential for establishing an appropriate prior in the generative model, ensuring biological plausibility when applied to repertoire-level analysis.

To the best of our knowledge, EpiGen represents the first sequence-to-sequence generative model for predicting epitopes from TCRs. We evaluated the generated epitopes across multiple dimensions, including binding affinities, chemical properties, and naturalness. The results show that the generated epitopes exhibit high binding affinities to the input TCRs and possess chemical properties similar to those of natural epitopes. In particular, most epitopes could be successfully matched to entries in known epitope databases. In repertoire-level evaluations, EpiGen generates diverse epitopes that conform to natural antigen category distributions. We next employ molecular dynamics simulations as an orthogonal evaluation method to deep learning-based affinity predictors, further corroborating the high binding affinities of the generated epitopes. Finally, we apply EpiGen to two practical scenarios: (1) identifying and quantifying tumor-associated $CD8^+$ T cells within the tumor microenvironment, and (2) characterizing COVID-19-associated $CD8^+$ T cells in peripheral blood mononuclear cell (PBMC) samples. EpiGen enables analyzing the abundance, clonal expansion, and differentially expressed genes of disease-associated $CD8^+$ T cells. Tumor-associated $CD8^+$ T cells in tumor patients, especially those clonally expanded in both tumor and normal adjacent tissue, exhibit significantly enhanced cytotoxic markers and reduced exhaustion signatures. These results support the previous hypothesis that tumor-specific $CD8^+$ T cells

are continuously replenished from the periphery. EpiGen identified COVID-19-associated T cells that showed clonal expansion and clear cytotoxic profiles in patients with mild and moderate symptoms. In contrast, COVID-19-specific T cells in severe patients retained naive and memory phenotypes rather than acquiring cytotoxic effector functions, potentially explaining the impaired viral control in these individuals. EpiGen enables more accurate quantification of T cell repertoires and potentially leads to novel insights into disease mechanisms.

2 Results

Developing a large-scale transformer to generate cognate epitopes EpiGen is a decoder-only transformer based on GPT-2[27]. EpiGen takes as input the CDR3β sequence of a TCR and outputs its potential cognate epitope sequences. The original GPT-2 model contains 1.5 billion parameters and was trained on natural language data derived from approximately 800 million Web pages. However, the currently available TCR-epitope binding pairs number $\sim 100,000$, which poses a significant challenge in training an effective deep learning model. To address this limitation, we utilized a label propagation scheme that incorporates high-confidence predicted TCR-epitope pairs as pseudo-labels for model training (**Fig. 1a**).

Pseudo-labeling assumes access to a reliable binding affinity predictor. We developed a highly competitive binding affinity predictor, named Robust Affinity Predictor (RAP), by modifying the head architecture, loss function, and data sampling strategies of TABR-BERT[23]. To minimize potential bias and improve model precision, we introduced Triple Negative Sampling, a technique that diversifies the sources of negative pairs. Given a set of paired data, the negative pairs are generated by randomly shuffling the paired data or pairing them with external TCRs or epitopes (**Methods**). The paired data were collected from four publicly available sources: VDJdb[35], IEDB[36], PIRD[37], and McPAS-TCR[38]. After preprocessing, the paired data were partitioned into training, validation, and test sets with a 7:2:1 ratio. Robust Affinity Predictor demonstrated superior or comparable performance to state-of-the-art models, including TABR-BERT, PanPep, and TEIM[24], as measured by the Area Under the Receiver Operating Curve (AUROC) and Area Under the Precision-Recall Curve (AUPRC) metrics, in multiple test sets (**Fig. 1b** and **Extended Data Fig. 1**).

We collected a pool of $7,331,478$ unique TCR sequences from TCRdb[39]. The 21,801,187 epitope sequences were obtained from three previous publications: NetMHCPan v4.0[40], MHCflurry v2.0[41], and SysteMHC[42] (**Supplementary Note 1**). In this study, we focus specifically on the binding between $CD8^+$ T cells and epitopes displayed on class I MHC molecules, while excluding interactions involving $CD4^+$ T cells and epitopes presented by class II MHC molecules. Class I MHC molecules bind and present short epitopes (8-12 amino acids) to $CD8^+$ T cells in a restricted manner, which warrants a focused modeling approach[43].

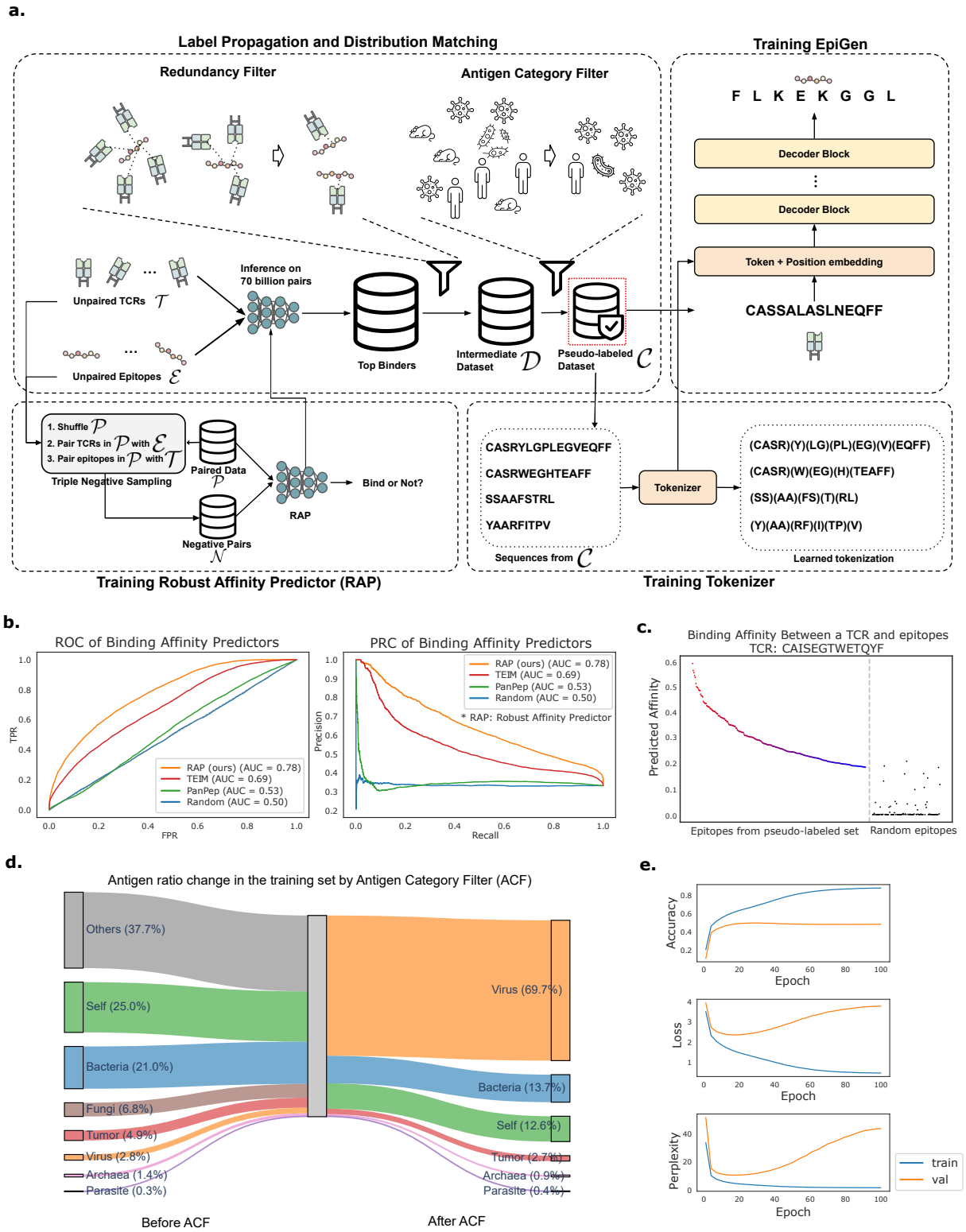
a.
Label Propagation and Distribution Matching
Redundancy Filter
Antigen Category Filter
Training EpiGen
F L K E K G G L
Decoder Block
Decoder Block
Token + Position embedding
CASSALASLNEQFF
Unpaired TCRs $\mathcal{T}$
Unpaired Epitopes $\mathcal{E}$
Inference on 70 billion pairs
Top Binders
Intermediate Dataset $\mathcal{D}$
Pseudo-labeled Dataset $\mathcal{C}$
1. Shuffle $\mathcal{P}$
2. Pair TCRs in $\mathcal{P}$ with $\mathcal{E}$
3. Pair epitopes in $\mathcal{P}$ with $\mathcal{T}$
Triple Negative Sampling
Paired Data $\mathcal{P}$
Negative Pairs $\mathcal{N}$
RAP
Bind or Not?
Training Robust Affinity Predictor (RAP)
CASRYLGPLEGVEQFF
CASRWEGHTEAFF
SSAAFSTRL
YAARFITPV
Sequences from $\mathcal{C}$
Tokenizer
(CASR)(Y)(LG)(PL)(EG)(V)(EQFF)
(CASR)(W)(EG)(H)(TEAFF)
(SS)(AA)(FS)(T)(RL)
(Y)(AA)(RF)(I)(TP)(V)
Learned tokenization
Training Tokenizer
b.
ROC of Binding Affinity Predictors
TPR
FPR
RAP (ours) (AUC = 0.78)
TEIM (AUC = 0.69)
PanPep (AUC = 0.53)
Random (AUC = 0.50)
PRC of Binding Affinity Predictors
Precision
Recall
RAP (ours) (AUC = 0.78)
TEIM (AUC = 0.69)
PanPep (AUC = 0.53)
Random (AUC = 0.50)
* RAP: Robust Affinity Predictor
c.
Binding Affinity Between a TCR and epitopes
TCR: CAISEGTWETQYF
Predicted Affinity
Epitopes from pseudo-labeled set
Random epitopes
d.
Antigen ratio change in the training set by Antigen Category Filter (ACF)
Others (37.7%)
Self (25.0%)
Bacteria (21.0%)
Fungi (6.8%)
Tumor (4.9%)
Virus (2.8%)
Archaea (1.4%)
Parasite (0.3%)
Virus (69.7%)
Bacteria (13.7%)
Self (12.6%)
Tumor (2.7%)
Archaea (0.9%)
Parasite (0.4%)
Before ACF
After ACF
e.
Accuracy
Epoch
Loss
Epoch
Perplexity
Epoch
train
val

Figure 1: **Overview of EpiGen development process based on label propagation and distribution matching a.** Core development process of EpiGen. Triple Negative Sampling was used to train Robust Affinity Predictor (RAP), which reliably predicts the binding affinity between a TCR and an epitope. Label propagation performs large-scale inference by randomly pairing unpaired TCRs and epitopes to find potential binders using RAP. Redundancy Filter and Antigen Category Filter ensure reduced redundancy and align the dataset with the expected antigen category distribution. The resulting pseudo-labeled data is used to train a tokenizer, which learns meaningful motifs of amino acids. The pseudo-labeled data and tokenizer are used to train a GPT-2 small model, which learns to generate epitope sequences from CDR3β inputs. **b.** ROC and PRC plots of binding affinity predictors, RAP (orange), TEIM (red), PanPep (green), Random (blue) on the test set merged from four publicly available datasets. The negative pairs were obtained by shuffling positive pairs. **c.** Binding affinity distribution for an example TCR "CAISEGTWETQYF" against epitopes from pseudo-labeled and random datasets. The y-axis shows binding affinity, while the x-axis shows epitope sources. Left shows the binding affinity between TCRs and the epitopes from pseudo-labeled data in decreasing order, and right shows the binding affinity between TCRs and arbitrary epitopes. **d.** Antigen category distribution in pseudo-labeled datasets before and after the application of Antigen Category Filter (ACF). Left: Pre-ACF distribution, with many other, self, and bacterial species as the dominant categories. Right: Post-ACF distribution, showing a shift to virus as the predominant category. Self and Tumor denote self-antigen and tumor-associated antigens, respectively. **e.** The learning curve of EpiGen. The average masked token prediction accuracy (top), loss (middle), and perplexity (bottom) values (y-axis) on the training and validation set are plotted by epoch (x-axis).

The pseudo-labeling process involved assessing the binding affinities of each unpaired TCR against 10,000 random epitopes sampled from a set of unpaired epitopes, identifying pairs exhibiting significantly higher affinities. As expected, the majority of TCR-epitope combinations showed negligible binding affinities; for example, the TCR sequence CAISEGTWETQYF exhibited a median binding affinity of 0.000 against randomly selected epitopes (**Fig. 1c**). However, we identified a subset of high-affinity interactions, with the top 256 predicted binders showing a median affinity of 0.429. To ensure specificity and reduce potential false positives, we filtered out promiscuous epitopes that were predicted to bind more than 100 different TCRs. This process, termed Redundancy Filter, was necessary to ensure the diversity of the generated epitopes. This systematic pseudo-labeling approach generated an intermediate dataset $\mathcal{D}$, containing 17 million TCR-epitope pairs.

A critical consideration in constructing the pseudo-labeled dataset was ensuring a biologically plausible distribution of antigen sources (e.g., viral, bacterial, and self-antigens). Although there are no universally accepted ratios for antigen-specific CD8$^+$ T cells, virus-specific cells often constitute a significant portion[44–46], while self-antigen and tumor-antigen-specific CD8$^+$ T cells generally occur at much lower frequencies in healthy individuals[47–50]. Our goal was to design a training set that effectively represented a large-scale TCR repertoire so that the model can learn not only the binding affinity relationships but also the natural distributional patterns. We developed the Antigen Category Filter (ACF) algorithm, which calibrates antigen distribution based on five fundamental immunological principles of CD8$^+$

T cells: (1) Viral Dominance, (2) Limited Bacterial Presence, (3) Endogenous Epitope Presence (Self-Antigen and Tumor-Associated Antigen), (4) Rare Fungi and Parasites, and (5) Absence of Pathogenic Archaea (**Methods**, **Supplementary Note 2**). Initial analysis of dataset $\mathcal{D}$ revealed that 37.7% and 25% of epitopes were derived from others (mostly Eukaryotic) and self-antigens, potentially introducing undesirable bias. After applying Antigen Category Filter, the resulting dataset $\mathcal{C}$, which we call Corpus, predominantly consisted of virus-associated epitopes (**Fig. 1d**).

We developed a custom tokenizer, trained on $\mathcal{C}$, to capture frequently occurring motifs in CDR3β and epitope sequences. The input sequences were processed using the tokenizer and augmented with positional embeddings for model training (**Methods**). The model architecture was a GPT-2-small, trained for 100 epochs using four NVIDIA L40S GPUs. The validation loss and perplexity initially decreased smoothly but began to increase after epoch 20 (**Fig. 1e**). The maximum next-token prediction accuracy reached 0.8843 (at epoch 100) and 0.5026 (at epoch 28) for the training and validation sets, respectively. To mitigate potential overfitting, we selected the model checkpoint from epoch 28 for subsequent analyses. For inference, we used top-k top-p sampling[51,52] as the decoding scheme to generate the most probable k tokens for a given input TCR, selecting from tokens whose cumulative probability reaches p to enhance diversity in the output.

EpiGen generates high-affinity and diverse epitopes We evaluated the binding affinities between the input TCRs and the generated epitopes across multiple test scenarios. We partitioned the test set of Corpus $\mathcal{C}$ into four subsets based on TCR and epitope exposure during training: UnseenEpi (TCRs seen, epitopes unseen), UnseenTCR (epitopes seen, TCRs unseen), SeenBoth (both seen, but not as a pair), and UnseenBoth (neither seen). EpiGen generated epitope sequences for each TCR in the test sets. We then measured the binding affinity between each TCR-epitope pair using the Robust Affinity Predictor. For comparison, we also measured the binding affinities between each TCR and 100 randomly sampled epitopes and calculated the percentile ranks of the binding affinities. The mean percentile ranks for UnseenEpi, UnseenTCR, SeenBoth, and UnseenBoth were 81.5, 81.3, 81.9, and 81.2, respectively (**Fig. 2a**). These results indicated that EpiGen can generate epitopes with high binding affinities for both previously encountered and novel TCRs.

We further evaluated EpiGen using test sets derived from four publicly available datasets: VDJdb, IEDB, PIRD, and McPAS-TCR. These test set splits were predetermined when developing the Robust Affinity Predictor. Two baselines were considered for comparison: RandGen and K-Nearest Neighbor (KNN). RandGen generates random amino acid sequences, with sequence lengths sampled from the empirical length distribution of epitopes in the training set. The KNN baseline identifies the closest TCR in the training set to the query TCR in terms of sequence similarity and returns the associated epitope.

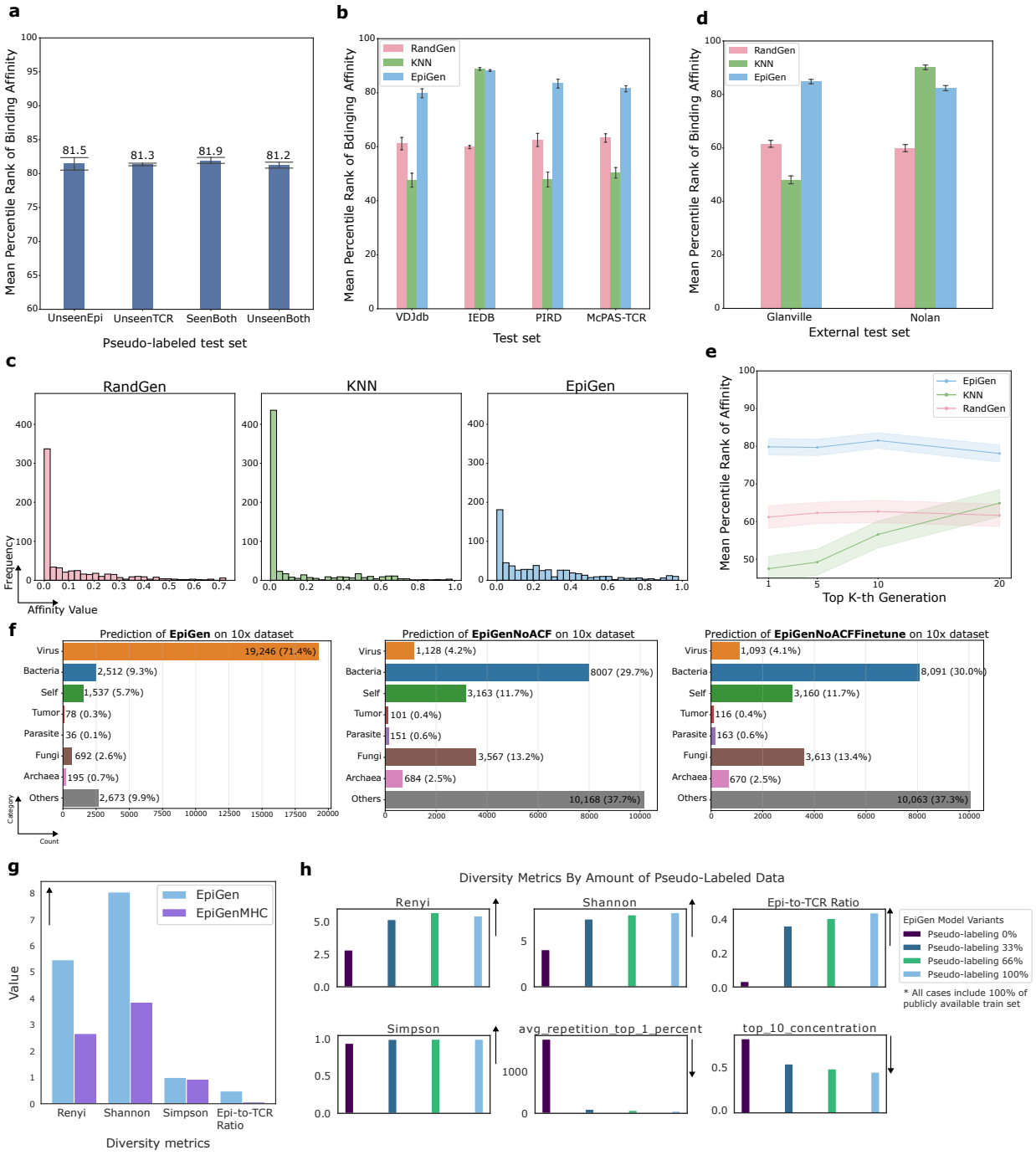
a
Mean Percentile Rank of Binding Affinity
81.5
81.3
81.9
81.2
UnseenEpi
UnseenTCR
SeenBoth
UnseenBoth
Pseudo-labeled test set
b
Mean Percentile Rank of Bdinging Affinity
RandGen
KNN
EpiGen
VDJdb
IEDB
PIRD
McPAS-TCR
Test set
d
Mean Percentile Rank of Binding Affinity
RandGen
KNN
EpiGen
Glanville
Nolan
External test set
c
RandGen
KNN
EpiGen
Frequency
Affinity Value
e
Mean Percentile Rank of Affinity
EpiGen
KNN
RandGen
Top K-th Generation
f
Prediction of EpiGen on 10x dataset
Virus 19,246 (71.4%)
Bacteria 2,512 (9.3%)
Self 1,537 (5.7%)
Tumor 78 (0.3%)
Parasite 36 (0.1%)
Fungi 692 (2.6%)
Archaea 195 (0.7%)
Others 2,673 (9.9%)
Category
Count
Prediction of EpiGenNoACF on 10x dataset
Virus 1,128 (4.2%)
Bacteria 8007 (29.7%)
Self 3,163 (11.7%)
Tumor 101 (0.4%)
Parasite 151 (0.6%)
Fungi 3,567 (13.2%)
Archaea 684 (2.5%)
Others 10,168 (37.7%)
Prediction of EpiGenNoACFFinetune on 10x dataset
Virus 1,093 (4.1%)
Bacteria 8,091 (30.0%)
Self 3,160 (11.7%)
Tumor 116 (0.4%)
Parasite 163 (0.6%)
Fungi 3,613 (13.4%)
Archaea 670 (2.5%)
Others 10,063 (37.3%)
g
EpiGen
EpiGenMHC
Value
Renyi
Shannon
Simpson
Epi-to-TCR Ratio
Diversity metrics
h
Diversity Metrics By Amount of Pseudo-Labeled Data
Renyi
Shannon
Epi-to-TCR Ratio
Simpson
avg_repetition_top_1_percent
top_10_concentration
EpiGen Model Variants
Pseudo-labeling 0%
Pseudo-labeling 33%
Pseudo-labeling 66%
Pseudo-labeling 100%
* All cases include 100% of publicly available train set

Figure 2: **Evaluation of the binding affinity, diversity, and distributional characteristics of the generated epitopes a.** Mean percentile rank (y-axis) of binding affinities between generated epitopes and query TCR sequences across four subsets of the pseudo-labeled test set (x-axis): UnseenEpi, UnseenTCR, SeenBoth, and UnseenBoth. For each generated epitope, 100 random epitopes were sampled to calculate the percentile rank of binding affinity. Error bars indicate 95% confidence intervals. Binding affinities were measured using Robust Affinity Predictor (RAP). **b.** Mean percentile rank (y-axis) of binding affinities between generated epitopes and query TCR sequences across test sets of four publicly available datasets (x-axis). For each generated epitope, 100 random epitopes were sampled to calculate the percentile rank. Error bars indicate 95% confidence intervals. Binding affinities were measured using Robust Affinity Predictor. **c.** Histogram comparing binding affinities of epitopes generated by RandGen, KNN, and EpiGen (x-axis). Results are based on the VDJdb test set. **d.** Mean percentile rank (y-axis) of binding affinities between generated epitopes and query TCR sequences across two external test sets (x-axis): Glanville et al., and Nolan et al. (MIRA). For each generated epitope, 100 random epitopes were sampled to calculate the percentile rank. Error bars indicate 95% confidence intervals. Binding affinities were measured using RAP. **e.** Mean percentile rank of binding affinities (y-axis) between query TCRs and top K generated epitopes (x-axis), evaluated at four K values (1, 5, 10, 20). Results compare performance of EpiGen, KNN, and RandGen. **f.** Distribution of antigen categories for epitopes generated by three model variants: EpiGen (left), EpiGenNoACF (middle), and EpiGenNoACFFinetune (right) using the 10x dataset. The 10x dataset is a repertoire-level dataset capturing $CD8^+$ T cell sequences from PBMCs of a healthy donor, distinct from aggregated samples from diverse sources. Self denotes self-antigens, and Tumor represents tumor-associated antigens. **g.** Bar plot comparing diversity indices (x-axis) of epitopes generated by EpiGen and EpiGenMHC. Diversity metrics include Renyi Diversity (α=2), Shannon Diversity, Simpson's Diversity, and Epi-to-TCR ratio, providing a comprehensive comparison of epitope diversity between the two models. Epi-to-TCR ratio is calculated as the number of uniquely generated epitopes divided by the number of TCRs. Results are based on the 10x dataset. The comparison demonstrates EpiGenMHC's inability to maintain epitope diversity when performing inference on a repertoire-level dataset. **h.** Bar plots comparing diversity indices of epitopes generated by model variants trained with varying amounts of pseudo-labeled data (0%, 33%, 66%, and 100%). Six diversity metrics were used: Rényi Diversity (α=2), Shannon Diversity, Simpson's Diversity, Epi-to-TCR ratio, avg_repetition_top_1_percent, and top_10_concentration. Epi-to-TCR ratio is given by the number of uniquely generated epitopes divided by the number of TCRs. avg_repetition_top_1_percent indicates the average repetition frequency of the top 1% generated epitopes, while top_10_concentration represents the proportion of total epitopes within the most frequent 10%. Results are based on the 10x dataset.

EpiGen-generated epitopes consistently demonstrated high performance in multiple evaluations. The mean percentile ranks of the binding affinities were close to or greater than 80% in all test sets. EpiGen outperformed RandGen and KNN on VDJdb, PIRD, and McPAS-TCR, while remaining competitive on IEDB (**Fig. 2b**). Furthermore, EpiGen-generated epitopes exhibited superior binding affinity values compared to those produced by the baseline methods (**Fig. 2c** and **Extended Data Fig. 2**).

EpiGen's performance was further assessed using external test sets derived from independent publications, comprising small-scale experimental datasets. These datasets were

independent of those used to train EpiGen or Robust Affinity Predictor. Details of the external test sets published by Glanville et al.[53] and Nolan et al.[54] are provided in **Supplementary Note 1**. EpiGen demonstrated robust performance, achieving mean percentile ranks of 85.8 and 84.1 on the Glanville et al. and Nolan et al. datasets, respectively (**Fig. 2d**).

Leveraging the ability of GPT-2 to produce multiple, slightly varied outputs for a single input, we analyzed the top 1, 5, 10, and 20 generations. In this extended evaluation, EpiGen consistently showed higher mean percentile ranks on public test sets compared to RandGen and KNN (**Fig. 2e**).

We further evaluated EpiGen's performance using repertoire-level test sets, specifically the 10x dataset[55] released by 10x Genomics, Inc., which contains paired RNA and TCR sequencing of $CD8^+$ T cells from a healthy donor. This evaluation is particularly valuable, as the dataset comprises TCR sequences measured from individual donors, resulting in a distinctive distribution compared to public test sets that aggregate TCRs from multiple independent studies. Therefore, this evaluation closely mirrors real-world application scenarios in which EpiGen is used to infer epitopes for an individual's entire TCR repertoire. For comparative analysis, we developed three additional variants of EpiGen: EpiGenNoACF, EpiGenNoACFFinetune, and EpiGenMHC. EpiGenNoACF was trained on the intermediate dataset $\mathcal{D}$ without applying Antigen Category Filter, thus lacking instruction on the proper distribution of antigen categories. EpiGenNoACFFinetune was derived by fine-tuning EpiGenNoACF using $\mathcal{C}$ to assess whether fine-tuning could effectively learn the distribution of antigen category while leveraging the larger intermediate dataset. EpiGenMHC incorporated both TCR and MHC information for epitope sequence generation. We evaluated the models in three key aspects: distribution of antigen categories of the generated epitopes, epitope diversity, and redundancy in multiple epitopes generated from the same TCR. Only models that demonstrated high performance across all three metrics were considered eligible for downstream analysis.

Analysis of EpiGen's output revealed that its generated epitopes predominantly originated from viruses (**Fig. 2f, left**), with biologically plausible proportions from tumoral, self, and bacterial sources. This distribution aligns with the immunological principles of Viral Dominance, Limited Bacterial Presence, and Endogenous Epitope Presence. In contrast, models trained without Antigen Category Filter (EpiGenNoACF and EpiGenNoACFFinetune) generated approximately 37.7% and 30% of epitopes from other (mostly Eukaryotic) and bacterial sources (**Fig. 2f, middle, right**), with notably fewer viral antigens. This skewed distribution reflects the initial bias in the dataset $\mathcal{D}$ prior to the application of Antigen Category Filter, highlighting the importance of our antigen category calibration approach.

To assess epitope diversity, we employed four diversity indices: Shannon Diversity[5], Rényi Diversity (α=2)[7], Simpson's Diversity[6], and the epi-to-TCR ratio. Shannon Diversity quantifies the entropy of epitope distribution, accounting for both the number of unique epitopes and their relative abundances. Rényi and Simpson's Diversity, which incorporate quadratic terms, are less sensitive to rare epitopes. The epi-to-TCR ratio is the total number of

uniquely generated epitopes divided by the number of unique input TCRs in the repertoire. EpiGen demonstrated superior epitope diversity, achieving an epitope-to-TCR ratio of 0.5 (**Fig. 2g**). In contrast, EpiGenMHC showed significantly lower diversity indices, indicating the generation of redundant epitopes for different TCRs. This limitation stems from the insufficient diversity of (TCR, epitope, MHC) triplets in the currently available datasets. Furthermore, EpiGen exhibited lower redundancy in its top 20 generations compared to EpiGenMHC (**Extended Data Fig. 3a**).

The analysis of epitope diversity provided crucial insight into the effects of label propagation. We evaluated models trained with different proportions of pseudo-labeled data: 0%, 33%, 66%, and 100% (denoted as Pseudo-labeling 0%, 33%, 66%, and 100%, respectively). The Pseudo-labeling 0% model, trained solely on the public paired dataset, exhibited severely limited epitope diversity, generating highly redundant sequences (**Fig. 2h**). We used two additional metrics: avg_repetition_top_1_percent, which measures the average repetition frequency of the top 1% generated epitopes, and top_10_concentration, which represents the proportion of total epitopes falling within the most frequent 10% epitope sequences. Pseudo-labeling 0% showed considerable redundancy, with the top 1% epitopes repeating approximately 2,000 times on average and a top_10_concentration exceeding 0.95. In contrast, Pseudo-labeling 100% achieved much greater diversity with a top_10_concentration below 0.50. Epitope diversity improved progressively with increasing proportions of pseudo-labeled data, highlighting the essential role of our label propagation algorithm in ensuring the generation of diverse epitopes. Moreover, redundancy in the top-k generations decreased gradually with higher proportions of pseudo-labeled data for training (**Extended Data Fig. 3b**).

Repertoire-level evaluations were instrumental in informing three key design choices: (1) implementing label propagation with Redundancy Filter, (2) applying Antigen Category Filter, which led to the exclusion of EpiGenNoACF and EpiGenNoACFFinetune, and (3) excluding MHC information, resulting in the removal of EpiGenMHC.

EpiGen generates natural epitopes We next examine the naturalness of the generated epitopes by comparing their various properties with those of naturally occurring epitopes collected from the test sets. The generated epitopes had an average length of 10.08, which aligns well with the typical length range[56] (8 to 12 amino acids) of the epitopes loaded onto MHC class I molecules (**Fig. 3a**). Additionally, the amino acid usage patterns of the generated epitopes closely resembled those of natural epitopes (Pearson correlation = 0.911; **Fig. 3b**).

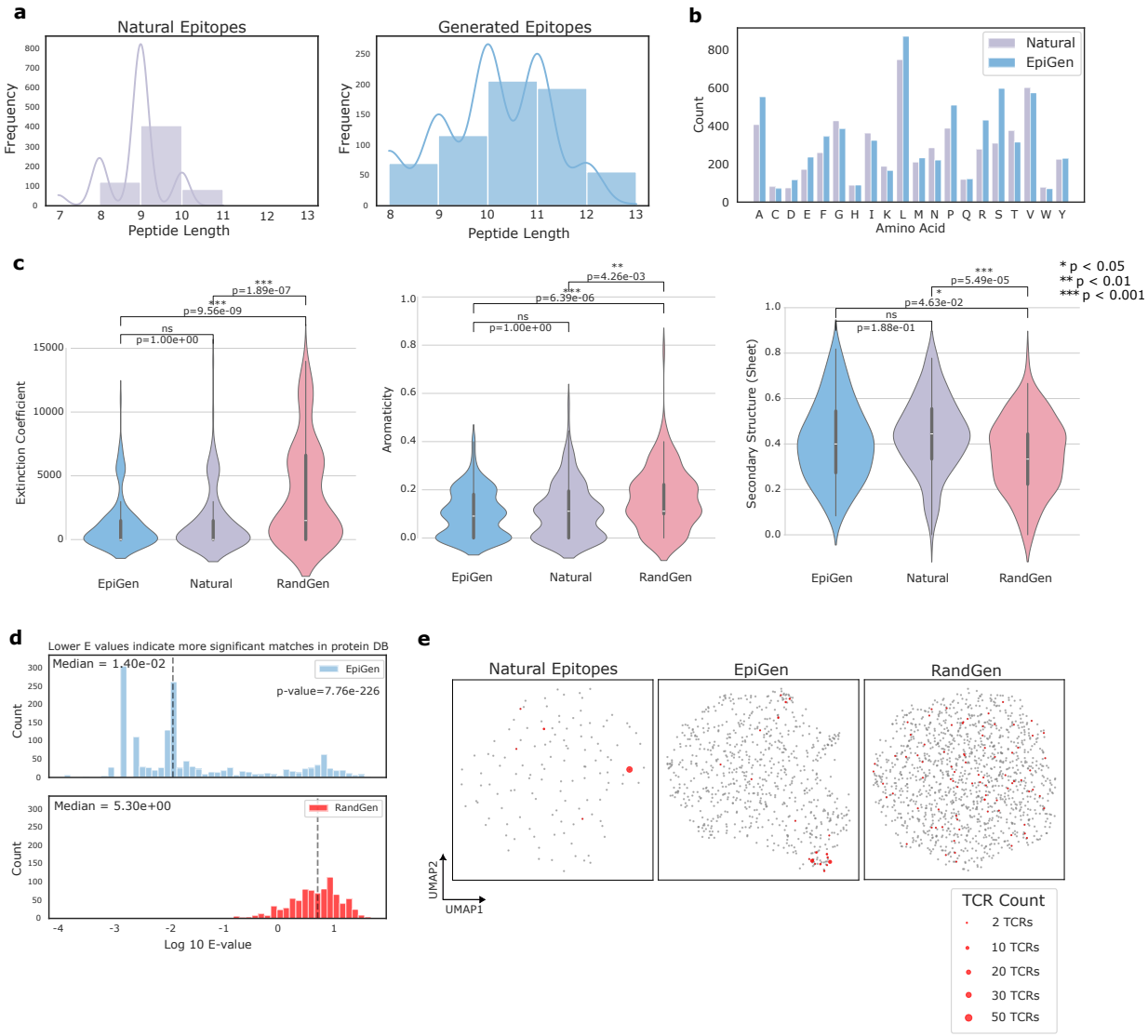
a
Natural Epitopes
Generated Epitopes
Frequency
Peptide Length
b
Natural
EpiGen
Count
Amino Acid
A C D E F G H I K L M N P Q R S T V W Y
c
Extinction Coefficient
Aromaticity
Secondary Structure (Sheet)
EpiGen
Natural
RandGen
ns
p=1.00e+00
p=9.56e-09
p=1.89e-07
p=6.39e-06
p=4.26e-03
p=1.88e-01
p=4.63e-02
p=5.49e-05
* p < 0.05
** p < 0.01
*** p < 0.001
d
Lower E values indicate more significant matches in protein DB
Median = 1.40e-02
p-value=7.76e-226
Median = 5.30e+00
Count
Log 10 E-value
e
Natural Epitopes
EpiGen
RandGen
UMAP2
UMAP1
TCR Count
2 TCRs
10 TCRs
20 TCRs
30 TCRs
50 TCRs

Figure 3: **Validation of naturalness of the epitopes generated by EpiGen a.** Length distribution comparison between natural epitopes (left) and EpiGen-generated epitopes (right) based on the VDJdb test set. Natural epitopes longer than 12 amino acids were excluded during preprocessing. **b.** Comparison of amino acid usage between natural epitopes (Natural) and EpiGen-generated epitopes. The distribution shows similar amino acid usage patterns between these groups based on the VDJdb test set, demonstrating the model's ability to replicate natural epitope characteristics. **c.** Distribution of chemical properties for epitopes from EpiGen (blue), Natural (purple), and RandGen (red). Natural epitopes were sampled from the VDJdb test set (n=642). Chemical properties include extinction coefficient, aromaticity, and secondary structure (sheet). Statistical significance was assessed using two-sided Mann-Whitney U tests with Bonferroni correction for multiple comparisons. Each violin plot contains an embedded box plot displaying the median, interquartile range (IQR), and whiskers extending to 1.5 x IQR. ns means 'not significant', *$p < 0.05$, **$p < 0.01$, and ***$p < 0.001$. Results demonstrate similarity in chemical properties between EpiGen-generated epitopes and natural epitopes. **d.** Distribution of BLASTP E-values for epitopes generated by EpiGen (blue, upper) and RandGen (red, lower). Each epitope was queried against the SwissProt database to identify source proteins. Lower E-values indicate higher statistical significance. Statistical comparison was performed using a one-sided Mann-Whitney U test. **e.** UMAP visualization of epitope space comparing Natural, EpiGen, and RandGen epitopes. Epitope similarity was computed using the BLOSUM62 matrix. Each dot represents an epitope, with dot size indicating number of paired TCRs. Colored dots represent epitopes recognized by TCRs sharing the GLIPH2 motif "CASSIRSQETQYF". Results are based on the PIRD test set, with Natural epitopes sampled from this set. The visualization demonstrates that similar EpiGen-generated epitopes are recognized by TCRs sharing GLIPH2 motifs.

To assess the chemical feasibility of the generated epitopes, we analyzed their several key properties using the `ProtParam` package[57]. We examined the extinction coefficient to evaluate the light-absorbing properties of the epitopes. Aromaticity was analyzed for its influence on hydrophobicity and potential interactions with TCRs. Secondary structure analysis provided insight into the potential folding tendencies of epitopes. We also considered isoelectric point to understand pH at which the epitopes carry no net electrical charge, which affects their behavior in different cellular environments. Finally, we evaluated instability index to gauge the stability of the epitopes in test tubes. The distributions of these chemical properties in EpiGen-generated epitopes closely mirrored those of natural epitopes, while randomly generated epitopes showed significantly different distributions (**Fig. 3c**). These trends were consistently observed in four independent public test sets (**Extended Data Fig. 4**).

The generated epitopes were queried against the SwissProt protein database using `blastp`[58] to assess the presence of significant matches (**Methods**). The significance of a `blastp` search is quantified by E-value, which represents the expected number of alignments with a score equal to or larger than the observed one by chance. The generated epitopes showed significantly lower E-values (Two-Tailed Mann-Whitney U test, $p=1.23 \times 10^{-244}$) compared to randomly generated epitopes, suggesting a significantly higher likelihood of identification within the database (**Fig. 3d**).

Natural and generated epitopes from the same test sets were qualitatively compared through visualization. Epitope embeddings were computed using pairwise BLOSUM similarity, followed by UMAP dimensionality reduction. Within each UMAP, epitopes paired with TCRs in the same motif group (defined using `GLIPH2`[10]) were color-highlighted. We observed that similar TCRs (in the same motif group) recognize similar epitopes (aggregated colored dots) in both natural epitopes and EpiGen-generated epitopes (**Fig. 3e, left, middle**). The colored dots representing EpiGen-generated epitopes showed localized aggregation with slight variation. These observations suggest that EpiGen produces diverse epitopes that extend beyond the range found in publicly available datasets while preserving recognition patterns of TCR motif groups. In contrast, the colored dots representing RandGen-generated epitopes appeared widely dispersed (**Fig. 3e, right**). These patterns were consistent across multiple TCR motif groups and datasets (**Extended Data Fig. 5**).

Recent protein language models, such as ProtGPT2[32], ProGen[59], and ProGen2[33], demonstrated protein sequence generation capabilities, but lack precise control mechanisms for specialized tasks such as the generation of $CD8^+$ T cell epitopes. Although ProGen incorporates conditioning through gene ontology keywords[60] and taxonomic tags, adapting these models for specific tasks such as TCR-specific epitope generation remains non-trivial. To evaluate the utility of pre-trained models, we fine-tuned ProGen2 on public training data across different learning rates. Our experiments revealed that fine-tuning with small learning rates (2e-5) produced unstable results (**Extended Data Fig. 6a**). The fine-tuned model frequently generated epitopes exceeding the biological length constraints, exhibiting a long-tailed length distribution (**Extended Data Fig. 6b**). This behavior stems from ProGen2's pre-training on general protein sequences, which are typically longer than T-cell epitopes that naturally range between 8 and 12 amino acids. Specifically, 4.41% of the generated sequences were longer than 12, while 1.47% were shorter than 8 amino acids. In contrast, training a GPT-2-small from scratch yielded more natural epitope length distributions and amino acid usage patterns (**Extended Data Fig. 6c**). When tested on the 10x dataset, the fine-tuned ProGen2 model exhibited severe bias, with 83.80% of generated sequences starting with 'G'. Furthermore, the model predicted an unnatural distribution of antigen categories in the 10x dataset, with Others, Bacteria, and Fungi dominating the predictions (**Extended Data Fig. 6d**). These findings suggest that strongly conditional generation tasks, where a single amino acid difference can significantly impact binding properties, require enhanced supervision through carefully curated training data that satisfy biological constraints.

EpiGen generates biophysically stable epitopes To analyze protein structures and interactions, we use Molecular Dynamics (MD) simulations, which compute molecular movements over time based on physical and statistical principles[61]. Specifically, we utilized `InterfaceAnalyzer`[62], from the `Rosetta` suite[63], to estimate TCR-pMHC complex binding affinity. For each CDR3β, EpiGen generated a corresponding epitope sequence. The complete 3D structure of the TCR-pMHC complex was then constructed using `TCRmodel2`[64], powered by AlphaFold2[65] (**Fig. 4a**). All simulations assumed the prevalent MHC allele HLA-A*02:01[66] and utilized a fixed TCR alpha chain (**Methods**). **Fig. 4b** shows an example of the 3D structure featuring an EpiGen-generated epitope, visualized using Mol*

Viewer[67]. The magnified interface between CDR3β (CAVSPLGGSQGNLIF) and the epitope (GILGFVFTLS) highlights a hydrogen bond between tyrosine in the epitope and glycine in the CDR3β, contributing to the stability of the complex.

We next evaluated the binding affinity of these complexes using two key metrics. Gibbs free energy (dG_separated) quantifies the energy difference before and after TCR-pMHC binding, providing a measure of binding affinity in an energy context[68]. Additionally, hydrophobic interactions, crucial forces in protein folding and docking[69], were also evaluated. For comparison, we sampled 20 random epitopes from the VDJdb test set as controls. EpiGen-generated epitopes showed lower Gibbs free energy compared to randomly sampled epitopes (**Fig. 4c, orange**), with a median percentile rank of 22.5%. This suggests that EpiGen-generated epitopes form more energetically stable complexes compared to randomly sampled ones. Furthermore, these epitopes exhibited pronounced hydrophobic interactions (**Extended Data Fig. 7**), with a mean percentile rank of 82.5%. This observation supports the idea that the generated epitopes form stronger hydrophobic interactions with the CDR3β region, potentially burying hydrophobic regions and contributing to binding stability. The natural epitopes from the test set showed a median percentile rank of 30.0% for Gibbs free energy, indicating that they also form more stable TCR-pMHC complexes than random control epitopes.

We analyzed seven additional properties and visualized the aggregated results (**Fig. 4d**). These properties include: binding free energy per unit area (dG_separated/dSASAx100), the number of unsatisfied hydrogen bonds at the interface (delta_unsatHbonds), interface energy scores for TCR and pMHC sides (side1_score and side2_score), normalized side scores (side1_normalized and side2_normalized), and total change in Solvent Accessible Surface Area (dSASA_int) (**Supplementary Note 3**).

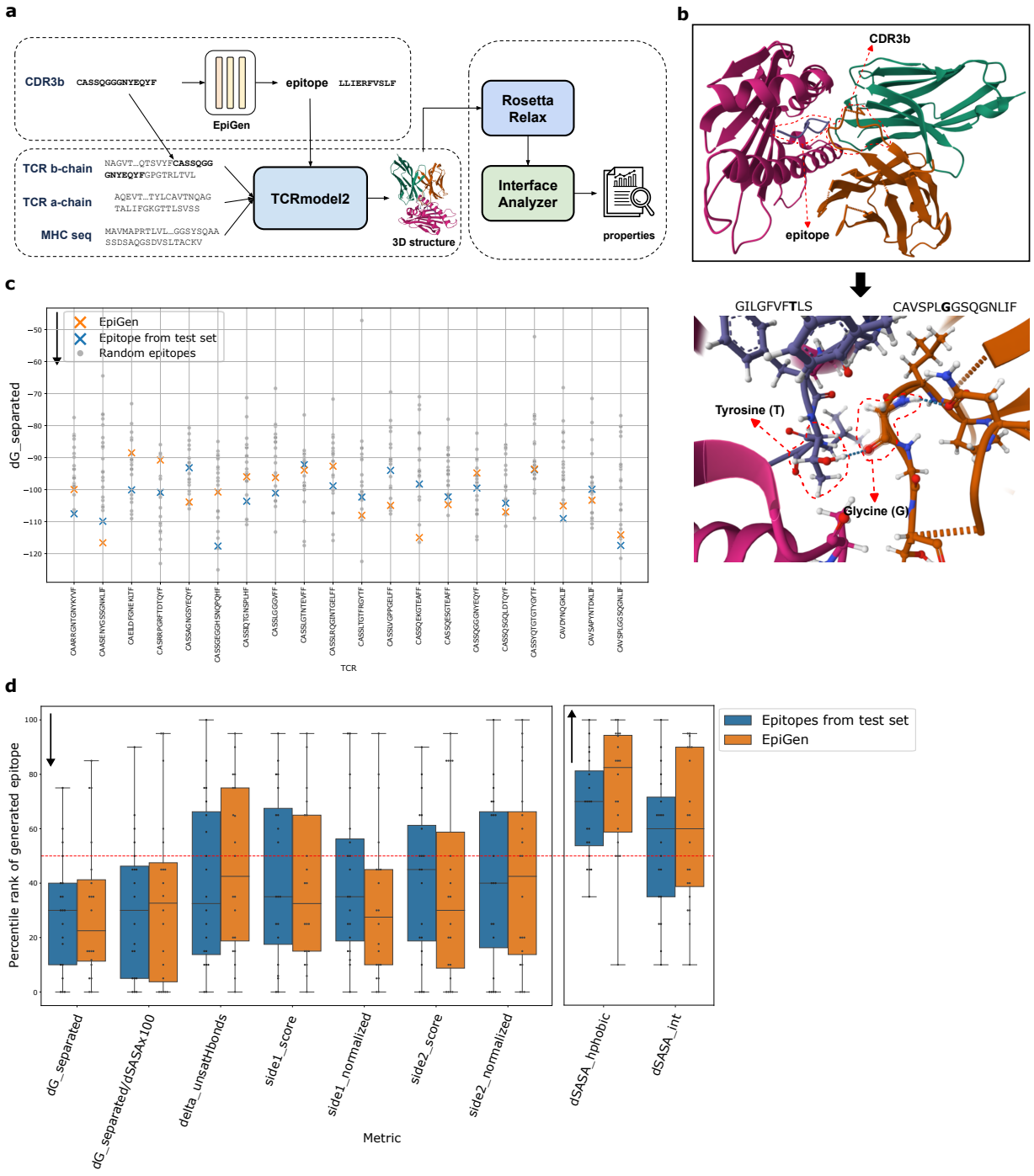
a
CDR3b
CASSQGGGNYEQYF
EpiGen
epitope
LLIERFVSLF
Rosetta Relax
TCR b-chain
NAGVT…QTSVYFCASSQGG GNYEQYFGPGTRLTVL
TCR a-chain
AQEVT…TYLCAVTNQAG TALIFGKGTTLSVSS
MHC seq
MAVMAPRTLVL…GGSYSQAA SSDSAQGSDVSLTACKV
TCRmodel2
3D structure
Interface Analyzer
properties
b
CDR3b
epitope
GILGFVFTLS
CAVSPLGGSQGNLIF
Tyrosine (T)
Glycine (G)
c
EpiGen
Epitope from test set
Random epitopes
dG_separated
TCR
d
Epitopes from test set
EpiGen
Percentile rank of generated epitope
dG_separated
dG_separated/dSASAx100
delta_unsatHbonds
side1_score
side1_normalized
side2_score
side2_normalized
dSASA_hphobic
dSASA_int
Metric

Figure 4: **Structural analysis on the TCR-pMHC complexes with the epitopes generated by EpiGen using InterfaceAnalyzer a.** A schematic showing the structural analysis pipeline. An epitope generated by EpiGen is fed to TCRmodel2, which outputs the 3D structure of the TCR-pMHC complex in PDB format. The file is analyzed using `Rosetta Relax` and `InterfaceAnalyzer`, which calculate diverse physicochemical properties. **b.** Visualization of the predicted 3D structure of a TCR-pMHC complex containing an epitope generated by EpiGen. The epitope and CDR3β of the TCR were highlighted. The CDR3β sequence was CAVSPLGGSQGNLIF, and the epitope sequence was GILGFVFTLS. The MHC allele HLA02:01 was used. The image is a screenshot taken from Mol* viewer. The lower image shows the detailed view of the TCR-pMHC interface. A hydrogen bond between the epitope's tyrosine and the CDR3β's glycine is highlighted, illustrating a potential binding mechanism for the generated epitope. **c.** Binding stability analysis of TCR-pMHC complexes. A scatter plot depicting dG_separated values (y-axis), for complexes containing EpiGen-generated epitopes (orange) or natural epitopes from the VDJdb test set (blue). dG_separated means the change in Rosetta energy when the interface-forming chains are separated, versus when they are complexed. Analysis was conducted across 20 TCRs (x-axis), with 20 random epitopes per TCR serving as controls (grey). Lower dG_separated values indicate higher structural stability in the energy context. dG_separated was calculated using `Rosetta`'s `InterfaceAnalyzer`. **d.** Comprehensive analysis of key physicochemical properties in TCR-pMHC complexes. Box plots depict the percentile ranks of nine physicochemical properties related to binding affinity for EpiGen-generated epitopes (orange) and natural epitopes from the test set (blue). Each dot represents the percentile rank of a property compared to 20 randomly sampled epitopes. The center red line (50%) indicates the performance of a random baseline. Properties were calculated using `Rosetta`'s `InterfaceAnalyzer`. Lower values of the first seven properties (dG_separated, dG_separated/dSASAx100, delta_unsatHbonds, side1_score, side1_normalized, side2_score, side2_normalized) and higher values of the last two properties (dSASA_hphobic, dSASA_int) indicate more stable structures or potentially stronger binding.

As a sanity check, epitopes from the test set shows mean percentile ranks below 50% on all energy-related properties (dG_separated, dG_separated/dSASAx100, side1_score, side1_normalized, side2_score, and side2_normalized) and delta_unsatHbonds. This aligns with our hypothesis that natural epitopes from the test set form more stable structures compared to randomly sampled epitopes. Notably, EpiGen-generated epitopes demonstrated similar trends across all properties, generally showing lower energy-related metrics. In contrast, both natural and generated epitopes displayed higher percentile ranks ($\geq$50%) on properties related to the interaction surface (dSASA_hphobic and dSASA_int). These results suggest that both natural and generated epitopes exhibit stronger interactions at the interface compared to those of random epitopes.

These findings indicate that EpiGen successfully captures key biophysical characteristics of natural epitopes, particularly in terms of energetic stability and hydrophobic interactions.

EpiGen discovers tumor-associated CD8$^+$ T cells CD8$^+$ tumor-infiltrating lymphocytes that recognize tumor-associated epitopes are central to cancer immunotherapy research[70]. To identify these tumor-reactive T cells, we performed computational inference on CDR3β sequences of CD8$^+$ T cells using EpiGen to predict their target epitopes. These

predicted epitopes were then cross-referenced against a curated database of known tumor-associated epitopes. T cells whose predicted epitopes matched entities in the database were classified as Phenotype-Associated (PA), while those without matches were designated Not-Associated (NA). For robustness, we took an ensemble of the predictions by three independently trained EpiGen models (**Supplementary Note 4**). Our underlying hypothesis was that PA T cells, compared to NA T cells, would exhibit enhanced activation signatures in tumor tissues due to their potential recognition of tumor-associated antigens. This EpiGen-based distinction of T cells into PA and NA populations enabled comprehensive differential analyses (**Fig. 5a**).

We used a dataset published by Wu et al.[71] which comprises paired single-cell RNA and TCR sequencing measurements in four types of cancer from three sites: tumor tissue, normal adjacent tissue (NAT), and peripheral blood. The study identified five $CD8^+$ T cell subsets: Teff (effector), Tem (effector memory), Trm-a, Trm-b, and Trm-c (tissue-resident memory cells, with cluster names shortened for brevity). Additionally, the study defined site patterns of TCRs based on their clonal expansion patterns in tumor tissue, NAT, and blood. We focused on three site patterns: Tumor Singleton (TCR observed only once in tumor tissue), Tumor Multiplet (TCR observed to be clonally expanded in tumor tissue), and Dual Expanded (TCR observed at least once in both tumor tissue and NAT) (**Fig. 5b**). 'All' means all cells were considered, regardless of their site patterns.

We first analyzed the prevalence of PA T cells in different cell subtypes and site patterns by calculating their proportion (PA ratio). PA ratios exhibited marked heterogeneity by cell subtypes: effector T cells (Teff) showed the highest ratio of 0.157, followed by effector memory T cells (Tem) with 0.122, while three subsets of tissue-resident memory T cells displayed lower ratios (Trm-a: 0.055, Trm-b: 0.072, Trm-c: 0.080) (**Fig. 5c, blue**). Analysis of tissue distribution patterns revealed that Dual Expanded cells exhibited notably elevated PA ratios in Teff and Tem populations (**Fig. 5c, red**), suggesting significant enrichment of putative effector-like tumor-associated $CD8^+$ T cell clones. The Tumor Multiplet pattern showed elevated PA ratios in Trm-a and Trm-b populations, though at lower levels than Teff and Tem cells. Trm-a and Trm-b cells show lower cytotoxic gene expression compared to Teff and Tem cells[71], which suggests potentially diminished anti-tumor efficacy by Tumor Multiplet than by Dual Expanded T cells. Notably, the enrichment of PA T cells within Dual Expanded populations supports the idea of recruitment of tumor antigen-specific $CD8^+$ T cells from peripheral sites. Consistent with their lack of clonal expansion, Tumor Singleton T cells showed the lowest PA ratios in Teff, Tem, and Trm-c subtypes. Based on these observations, EpiGen enables direct computational assessment of PA T cell abundance, providing an efficient alternative to traditional, labor-intensive biological assays.

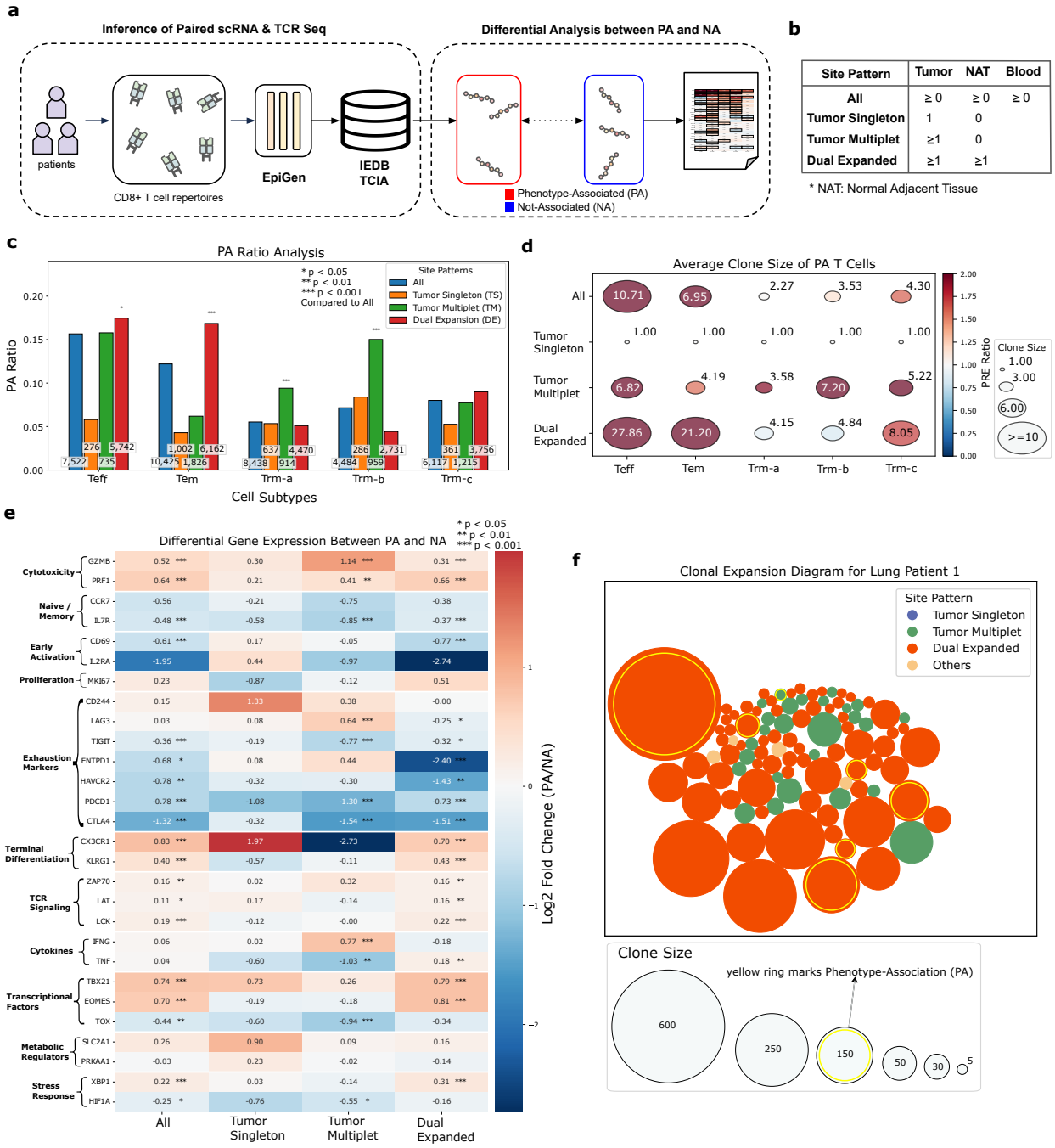
a
Inference of Paired scRNA & TCR Seq
Differential Analysis between PA and NA
patients
CD8+ T cell repertoires
EpiGen
IEDB
TCIA
Phenotype-Associated (PA)
Not-Associated (NA)
b
Site Pattern | Tumor | NAT | Blood
All | ≥ 0 | ≥ 0 | ≥ 0
Tumor Singleton | 1 | 0
Tumor Multiplet | ≥1 | 0
Dual Expanded | ≥1 | ≥1
* NAT: Normal Adjacent Tissue
c
PA Ratio Analysis
* p < 0.05
** p < 0.01
*** p < 0.001
Compared to All
Site Patterns
All
Tumor Singleton (TS)
Tumor Multiplet (TM)
Dual Expansion (DE)
PA Ratio
Teff
Tem
Trm-a
Trm-b
Trm-c
Cell Subtypes
d
Average Clone Size of PA T Cells
All
Tumor Singleton
Tumor Multiplet
Dual Expanded
PRE Ratio
Clone Size
e
Differential Gene Expression Between PA and NA
* p < 0.05
** p < 0.01
*** p < 0.001
Cytotoxicity
Naive / Memory
Early Activation
Proliferation
Exhaustion Markers
Terminal Differentiation
TCR Signaling
Cytokines
Transcriptional Factors
Metabolic Regulators
Stress Response
GZMB
PRF1
CCR7
IL7R
CD69
IL2RA
MKI67
CD244
LAG3
TIGIT
ENTPD1
HAVCR2
PDCD1
CTLA4
CX3CR1
KLRG1
ZAP70
LAT
LCK
IFNG
TNF
TBX21
EOMES
TOX
SLC2A1
PRKAA1
XBP1
HIF1A
All
Tumor Singleton
Tumor Multiplet
Dual Expanded
Log2 Fold Change (PA/NA)
f
Clonal Expansion Diagram for Lung Patient 1
Site Pattern
Tumor Singleton
Tumor Multiplet
Dual Expanded
Others
Clone Size
yellow ring marks Phenotype-Association (PA)

Figure 5: **Comparative analysis of Phenotype-Associated (PA) and Not-Associated (NA) T cells by different site patterns in cancer patients a.** Schematic of the analysis pipeline. EpiGen generates potential epitopes for $CD8^+$ cells from paired single-cell RNA and TCR sequencing data. Epitopes are queried against IEDB and TCIA databases to assess tumor association. TCRs and corresponding epitopes are then classified as Phenotype-Associated (PA) or Not-Associated (NA), followed by differential analyses between these groups. **b.** Summary of T cell clone distribution patterns across Tumor, Normal Adjacent Tissue (NAT), and Blood. Three patterns were defined based on clone size: Tumor Singleton, Tumor Multiplet, and Dual Expanded. An additional category, 'All,' was included where all cells were considered, regardless of their site patterns. Modified from Wu et al. **c.** Proportions of Phenotype-Associated (PA) TCRs within T cell repertoires, stratified by cell subtype (Teff, Tem, Trm-a, Trm-b, Trm-c) and site pattern (All, Tumor Singleton, Tumor Multiplet, Dual Expanded). One-sided Fisher's exact tests were performed to test the enrichment of PA T cells in each site pattern to the 'All' category within each cell subtype. P-values were adjusted using the Benjamini–Hochberg method (*$p < 0.05$, **$p < 0.01$, ***$p < 0.001$). Sample sizes (n) for each site pattern and cell subtype are shown in each bar. **d.** Mean clone size of Phenotype-Associated (PA) TCRs by cell subtype (x-axis) and site pattern (y-axis). Color intensity indicates the Phenotype-Relative Expansion (PRE) ratio, which is the mean clone size of PA T cells divided by that of NA T cells. Red indicates a larger PRE ratio. Circle size represents the mean clone size of PA T cells. Significant differences between clone sizes of PA and NA T cells were assessed using a one-sided Mann-Whitney U test, with p-values corrected for multiple testing via the Benjamini–Hochberg method. Only significant p-values are shown. Sample sizes (n) for site patterns [All, Tumor Singleton, Tumor Multiplet, Dual Expanded]: Teff (n = 7522, 276, 735, 5742), Tem (n = 10425, 1002, 1826, 6162), Trm-a (n = 8438, 637, 914, 4470), Trm-b (n = 4484, 286, 959, 2731), and Trm-c (n = 6117, 361, 1215, 3756). The numbers of PA T cells for site patterns [All, Tumor Singleton, Tumor Multiplet, Dual Expanded]: Teff (1178, 16, 116, 1003), Tem (1272, 43, 113, 1039), Trm-a, (466, 34, 86, 228), Trm-b (321, 24, 144, 121), and Trm-c (490, 19, 94, 338). **e.** Heatmap of differential gene expression between Phenotype-Associated (PA) and Not-Associated (NA) TCRs, ranked by magnitude of difference. Statistical tests were performed using a two-sided Wilcoxon rank-sum test from Scanpy, and p-values were adjusted for multiple testing using the Benjamini-Hochberg method (*$p < 0.05$, **$p < 0.01$, ***$p < 0.001$). Analysis was performed for four site patterns (x-axis): All, Tumor Singleton, Tumor Multiplet, and Dual Expanded. The curated gene list was obtained from Wu et al., containing genes related to $CD8^+$ T cells subtypes, states, and activation. **f.** $CD8^+$ T cell composition in Lung Patient 6, combining data from lung tumor tissue, Normal Adjacent Tissue (NAT), and blood data. The top 100 expanded clones are shown, with circle size representing clone size and color denoting cell subtype. Phenotype-Associated (PA) T cells are marked with yellow rings. The plot provides an overview of the clonal expansion patterns and tumor-associated T cells.

We next investigated the differential clonal expansion patterns between PA and NA T cells by introducing the Phenotype-Relative Expansion (PRE) ratio, defined as the ratio of average clone sizes between PA and NA TCRs. A PRE ratio of 1.0 indicates equivalent clonal expansion between PA and NA populations. PRE ratios were calculated across cell subtypes and site patterns (**Fig. 5d**). Notably, all T cell subtypes exhibited PRE ratios exceeding 1.0 in the aggregate analysis (**Fig. 5d, All**), consistent with the established prin-

ciple that antigen-specific CD8$^+$ cells undergo preferential clonal expansion after antigen recognition[72]. Although single tumor cells showed uniform PRE ratios of 1.0 by definition, Dual Expanded cells (especially Teff and Tem) showed markedly elevated PRE ratios, suggesting coordinated clonal expansion in both tumor tissue and normal adjacent tissue in response to tumor antigens. Tumor Multiplet cells also showed high PRE ratios across all cell subtypes. Patient-specific analysis revealed substantial heterogeneity in clonal expansion patterns (**Extended Data Fig. 8**). Several patients (Lung Patient 1, Lung Patient 2, Renal Patient 2, and Lung Patient 4) exhibited pronounced PRE ratios in Dual Expanded cells, with distinct distributions across T cell subtypes (**Extended Data Fig. 8a-d**). For example, Lung Patient 1 showed high PRE ratios in Teff, Tem, and Trm-a cells, while Lung Patient 4 showed elevated ratios in Teff and Trm-c cells. In contrast, Renal Patient 1 and Lung Patient 6 showed minimal clonal expansion across all cell subtypes (**Extended Data Fig. 8e,f**). These results reveal that T cell populations vary widely in both their clonal expansion patterns and antigen recognition capabilities, aligned with previous findings by Yost et al.[73]. This quantitative approach to measuring antigen recognition heterogeneity provides a valuable new tool for assessing disease status and stratifying patients.

Differential gene expression analysis between PA and NA CD8$^+$ T cell clones revealed distinct transcriptional signatures associated with antigen specificity (**Fig. 5e**). In the aggregate analysis (**Fig. 5e, All**), PA T cells exhibited enhanced cytotoxic potential, characterized by upregulation of genes encoding cytolytic effector molecules (*GZMB*, *PRF1*), TCR signaling components (*ZAP70*, *LAT*, *LCK*), and effector-associated transcription factors (*TBX21*, *EOMES*), while showing decreased expression of multiple exhaustion markers (*TIGIT*, *ENTPD1*, *HAVCR2*, *PDCD1*, *CTLA4*). This molecular signature was similarly observed in Dual Expanded T cells - populations showing clonal expansion in both tumor and normal adjacent tissue - which displayed heightened expression of cytotoxic effector molecules (*GZMB*, *PRF1*, *TNF*) and terminal differentiation markers (*KLRG1*), coupled with reduced expression of multiple exhaustion markers. This transcriptional profile mirrors that of recently activated effector memory/effector T cells (T_{EMRA}) described by Zhang et al.[74], which exhibited clonal expansion across blood, normal tissue, and tumor tissue with distinctive tumor-specific TCR repertoires. In contrast, Tumor Multiplet PA T cells, while maintaining high expression of cytolytic molecules (*GZMB*, *PRF1*) and cytokines (*IFNG*), showed a mixed exhaustion phenotype (elevated *LAG3* but downregulated *TIGIT*, *PDCD1*, *CTLA4*) and decreased *TNF* expression. Unlike their Dual Expanded counterparts, these cells lacked upregulation of TCR signaling markers and key transcription factors. The enhanced activation signatures observed in Dual Expanded PA T cells may explain the superior response to immune checkpoint inhibitors in patients with prominent Dual Expanded T cell signatures[71]. These molecular insights validate EpiGen's predictive capabilities and illuminate the transcriptional programs underlying effective anti-tumor T cell responses.

To characterize expanded T cell clones, we visualized the top 100 clonally expanded CD8$^+$ T cells per patient, mapping their spatial distribution, clone size, and phenotype (PA TCRs marked by yellow rings). These visualizations revealed different patterns of T cell repertoire in patients. Lung Patient 6 and Renal Patient 2 showed predominantly Dual Expanded

PA TCRs, indicating active replenishment of tumor-recognizing T cells from adjacent tissue (**Fig. 5f**, **Extended Data Fig. 9a**). In contrast, the repertoire of Colon Patient 2 consisted mainly of Tumor Singleton and Tumor Multiplet T cells (**Extended Data Fig. 9b**). Lung Patient 3 exhibited both patterns associated with the immunotherapy response: clonally expanded PA T cells in Dual Expanded and Tumor Multiplet patterns, suggesting complementary anti-tumor mechanisms[71] (**Extended Data Fig. 9c**). Lung Patient 5 showed numerous Dual Expanded and Tumor Multiplet T cells but limited PA T cell expansion (**Extended Data Fig. 9d**). These varying distributions of tumor-specific and bystander T cells align with previous findings[75]. EpiGen-based identification of PA and NA T cells enables quantification of T cell activation states within the tumor microenvironment and captures interpatient heterogeneity, potentially informing personalized immunotherapy strategies[30,76,77].

Sensitivity analyses of EpiGen demonstrated the robustness of our findings across various parameter settings. Specifically, our observations from the tumor dataset remained consistent when varying the number of epitopes generated per TCR (K) and the relative proportions of antigen categories in the Antigen Category Filter (**Supplementary Note 4**).

EpiGen characterizes COVID19-associated CD8$^+$ T cells EpiGen was used to characterize COVID-19-associated CD8$^+$ T cells using the data from Su et al.[78]. This study provided paired RNA and TCR sequencing data of blood samples from 139 donors, classified into four groups according to the WHO Ordinal Scale (WOS): healthy controls (WOS=0, no viral infection), mild cases (WOS=1-2, ambulatory with limited symptoms), moderate cases (WOS=3-4, hospitalized, potentially requiring supplemental oxygen), and severe cases (WOS=5-7, hospitalized requiring advanced respiratory support). Our analysis focused on CD8$^+$ T cells. Seven major cell clusters were identified and consolidated into four subtypes based on the gene signatures described by Su et al. (**Methods**): naive, memory, effector, and proliferative (**Fig. 6a**). The distribution of these subtypes varied with the severity of the disease. Healthy individuals exhibited a predominance of naive cells, while mild cases showed a more balanced distribution of cell subtypes. As the disease severity increased, the T cell populations shifted, with moderate cases dominated by effector cells and severe cases characterized by a prevalence of proliferative cells. These results indicate a dynamic remodeling of T cell populations in response to increasing COVID-19 severity[78].

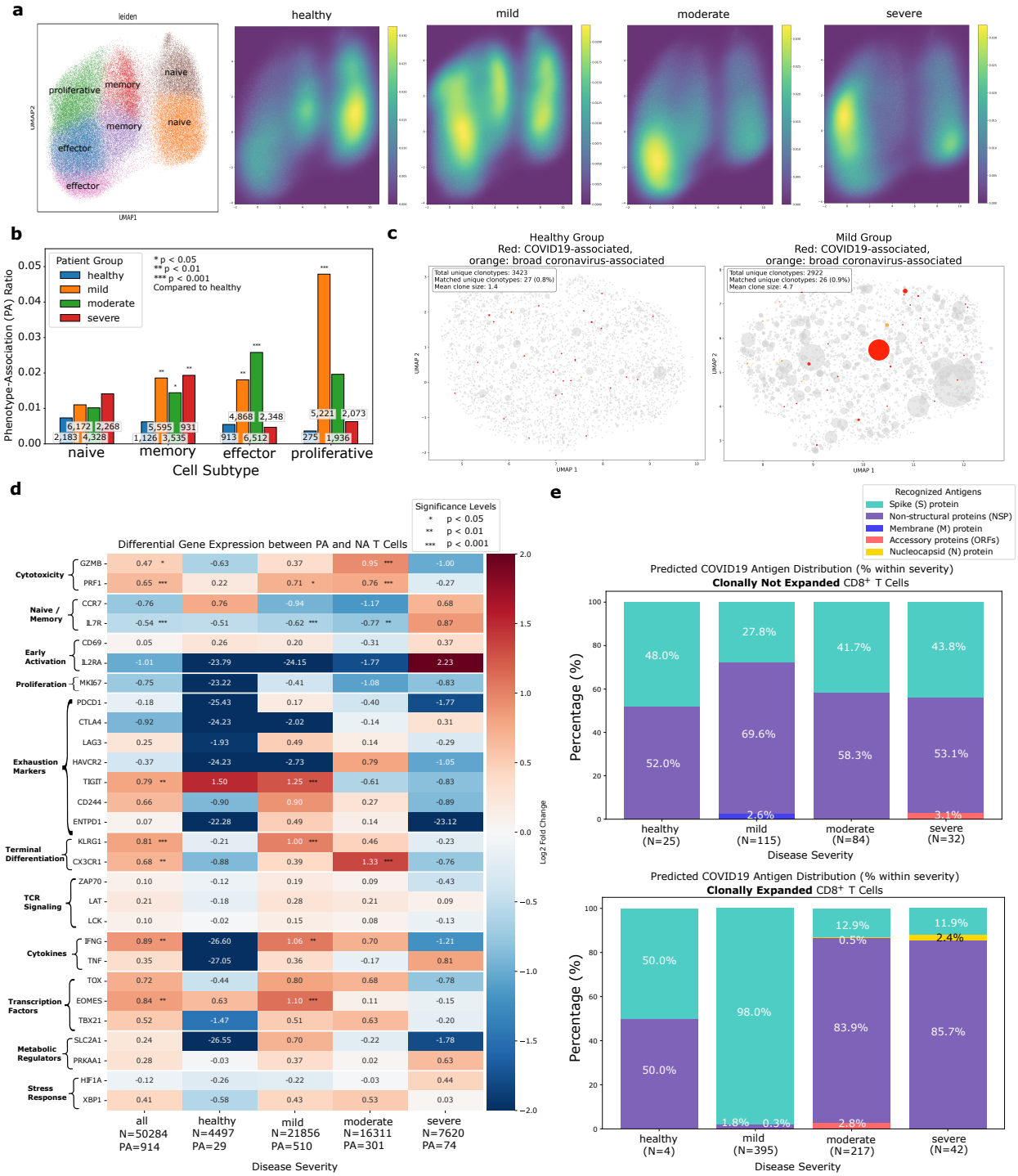
a
leiden
proliferative
memory
naive
memory
naive
effector
effector
UMAP1
UMAP2
healthy
mild
moderate
severe
b
Patient Group
healthy
mild
moderate
severe
* p < 0.05
** p < 0.01
*** p < 0.001
Compared to healthy
Phenotype-Association (PA) Ratio
naive
memory
effector
proliferative
Cell Subtype
c
Healthy Group
Red: COVID19-associated,
orange: broad coronavirus-associated
Mild Group
Red: COVID19-associated,
orange: broad coronavirus-associated
UMAP 1
UMAP 2
d
Differential Gene Expression between PA and NA T Cells
Significance Levels
* p < 0.05
** p < 0.01
*** p < 0.001
Cytotoxicity
Naive / Memory
Early Activation
Proliferation
Exhaustion Markers
Terminal Differentiation
TCR Signaling
Cytokines
Transcription Factors
Metabolic Regulators
Stress Response
GZMB
PRF1
CCR7
IL7R
CD69
IL2RA
MKI67
PDCD1
CTLA4
LAG3
HAVCR2
TIGIT
CD244
ENTPD1
KLRG1
CX3CR1
ZAP70
LAT
LCK
IFNG
TNF
TOX
EOMES
TBX21
SLC2A1
PRKAA1
HIF1A
XBP1
all N=50284 PA=914
healthy N=4497 PA=29
mild N=21856 PA=510
moderate N=16311 PA=301
severe N=7620 PA=74
Disease Severity
Log2 Fold Change
e
Recognized Antigens
Spike (S) protein
Non-structural proteins (NSP)
Membrane (M) protein
Accessory proteins (ORFs)
Nucleocapsid (N) protein
Predicted COVID19 Antigen Distribution (% within severity)
Clonally Not Expanded CD8+ T Cells
Percentage (%)
healthy (N=25)
mild (N=115)
moderate (N=84)
severe (N=32)
Disease Severity
Predicted COVID19 Antigen Distribution (% within severity)
Clonally Expanded CD8+ T Cells
healthy (N=4)
mild (N=395)
moderate (N=217)
severe (N=42)

Figure 6: **Comparative analysis of Phenotype-Associated (PA) and Not-Associated (NA) TCRs in the paired scRNA and TCR sequencing data measured from COVID-19 patients with varying severity a.** UMAP visualization of $CD8^+$ T cells based on gene expression data, clustered using the Leiden algorithm (resolution 1.0). Colors represent distinct clusters. Four distinct cell types were identified: naive, memory, effector, and proliferative. Adjacent heatmaps illustrate cluster prevalence across patient groups: healthy, mild, moderate, and severe (from left to right). Heatmaps were generated using Gaussian kernel density estimation. **b.** Proportions of COVID-19-associated TCRs (PA ratio) across patient severity groups (healthy, mild, moderate, severe) and T cell subtypes (naive, memory, effector, proliferative). PA ratio is defined as the number of COVID-19-associated TCRs divided by the total TCR count in each group. One-sided Fisher's exact tests were performed to compare PA proportions of each severity group to the healthy control within each cell subtype. P-values were adjusted using the Benjamini–Hochberg method (*$p < 0.05$, **$p < 0.01$, ***$p < 0.001$). The sample sizes (n) for both patient groups and cell subtypes are indicated on each corresponding bar. **c.** UMAP visualization of TCR sequences from $CD8^+$ T cells in healthy and mild groups. Sequence similarity was calculated using the BLOSUM62 substitution matrix. Predicted epitope sequences from TCRs, inferred using EpiGen, were queried against the curated IEDB database to determine phenotype associations. COVID-19-associated TCRs are shown in red, and broad coronavirus-associated TCRs are in orange. Both plots analyzed the same number of TCRs (4,497). The legend (upper left) displays the total number of clonotypes, COVID-19-associated clonotypes, and the mean clone size. **d.** Heatmap showing differential gene expression between Phenotype-Associated (PA) and Not-Associated (NA) TCRs, grouped by gene functions relevant to $CD8^+$ T cells. The analysis was performed across five patient groups: all, healthy, mild, moderate, and severe. Differential gene expression was assessed using the two-sided Wilcoxon rank-sum test from Scanpy, and p-values were adjusted for multiple testing using the Benjamini-Hochberg method (*$p < 0.05$, **$p < 0.01$, ***$p < 0.001$), with log2 fold changes plotted in color scale. **e.** Antigen distribution of Phenotype-Associated (PA) epitopes across patient groups, as identified by EpiGen. The stacked bar plots show antigen proportions for COVID-19 antigens (indicated by distinct colors) in two analyses: (top) proportions based on non-expanded $CD8^+$ T cells, and (bottom) proportions based on clonally expanded $CD8^+$ T cells.

EpiGen was used to generate the eight most probable epitopes for each T cell based on its CDR3β sequence. T cells were labeled as PA if any of their generated epitopes matched entries in a curated database of COVID-19-associated epitopes; otherwise, they were labeled as NA. For robustness, we took an ensemble of the predictions by three independently trained EpiGen models. We first investigated PA ratios by disease severity. The overall frequency of PA T cells was approximately 1% of the total $CD8^+$ T cell population (**Fig. 6b**). Healthy individuals exhibited consistently low PA ratios in all cell subtypes, likely due to reduced detection of unexpanded PA cell clones. In contrast, mild cases - patients who could effectively control COVID-19 without hospitalization - demonstrated elevated PA ratios in memory, effector, and proliferative populations. This suggests that the abundance of antigen-specific T cells enables efficient control of COVID-19 as observed in previous studies[79]. Similarly, moderate cases maintained high PA ratios in memory and effector populations. However, severe cases showed markedly reduced PA ratios in both effector and proliferative populations, indicating a deficiency in COVID-19-recognizing effector-like

T cells (**Fig. 6b, severe**). This result is consistent with multiple previous studies that observed lymphophenia and insufficient CD8$^+$ T cell responses in severe patients[80].

We investigated the clonal dynamics of PA T cells by performing a comparative analysis of the TCR repertoires between healthy individuals and patients with mild COVID-19. To ensure unbiased comparison, we randomly sampled equal numbers of TCRs from each group. TCR similarities were quantified using the sequence alignment and the BLOSUM62 substitution matrix[81], followed by UMAP dimensionality reduction. In the resulting visualization, each point represents a unique T cell clone, with point size proportional to the clonal size (**Fig. 6c**). The predicted TCRs to recognize COVID-19-specific epitopes were colored red, while those associated with broader coronavirus epitopes were colored orange to assess potential cross-reactivity. Our analysis revealed different patterns of PA T cell clonal expansion according to disease severity. Although healthy controls showed minimal clonal expansion, mild cases showed pronounced expansion of PA T cells, suggesting robust viral antigen-driven clonal expansion[82,83]. The average clone size peaked in the mild group, followed by a progressive decrease in the moderate and severe groups. This indicates effective recognition of COVID-19 epitopes and subsequent clonal expansion in mild and moderate patients but not in severe patients. Notably, the severe group showed a smaller average clone size in PA T cells compared to background T cells, suggesting an impaired ability to mount CD8$^+$ T cell clonal expansion against SARS-CoV-2 infection (**Extended Data Fig. 10a-c**). In particular, T cells predicted to recognize broader coronavirus epitopes showed a similar severity-dependent expansion pattern, while background (NA) TCRs consistently maintained small average clone sizes. These findings suggest that both COVID-19-specific and cross-reactive T cell responses may contribute to disease progression through differential clonal expansion patterns[84,85]. These results validate both the robustness and the utility of EpiGen in analyzing independent single-cell TCR repertoire data with minimal assumptions.

Next, we analyzed differential gene expression between PA and NA cells by severity group, visualizing log2 fold changes for genes of interest (**Fig. 6d**). In the aggregate analysis, PA T cells exhibited significantly elevated expression of cytolytic molecules (*GZMB*, *PRF1*), migration markers (*CX3CR1*), antiviral cytokines (*IFNG*), and transcription factors (*EOMES*) (**Fig. 6d, All**), indicating a distinct effector phenotype with enhanced cytotoxic characteristic of active antiviral responses. The presence of exhaustion markers suggested chronic antigenic stimulation in these cells. Mild cases maintained this molecular signature, which could explain their effective viral control. This phenotype is similar to clonally expanded and effector-like CD8$^+$ T cells observed in acute COVID-19 infection associated with improved clinical outcomes[80,86]. PA T cells in moderate cases demonstrated a high cytotoxic potential (*GZMB*, *PRF1*) with potentially reduced exhaustion compared to mild cases, along with elevated expression of the chemokine receptor gene *CX3CR1*, suggesting potential migration to inflamed lung tissue. Notably, PA T cells in severe cases lacked characteristic cytotoxic signatures and maintained expression of naive/memory markers, indicating impaired cytotoxic function, T cell dysfunction, or aberrant differentiation. Our observation further supports and details the findings of Su et al.[78], who showed that patients with severe symptoms exhibited an increase in naive T cell clusters while showing a decrease in activated effector T

cells compared to patients with moderate symptoms.

Analysis of the distributions of the generated epitopes revealed distinct antigen recognition patterns across COVID-19 severity groups. Non-expanded T cell clones maintained balanced recognition profiles between structural and non-structural proteins[87,88] across all severity groups, suggesting preserved immune surveillance capacity (**Fig. 6e, top**). In contrast, expanded clones showed marked differences between mild cases and moderate/severe cases. Mild cases exhibited substantial spike protein targeting (98% of expanded clones), while moderate and severe cases displayed a strong skew toward non-structural protein recognition (**Fig. 6e, bottom**). This skew could potentially serve as a predictive marker for disease progression, complementing existing findings on T cell exhaustion signatures in severe COVID-19[89,90]. The higher proportion of spike-specific T cells in mild cases compared to moderate (12.9%) and severe cases (11.9%) highlights the importance of structural protein recognition by $CD8^+$ T cells in viral control, not only by $CD4^+$ T cells, addressing a gap noted in previous studies[91–93]. These findings suggest that proper clonal expansion of $CD8^+$ T cells that recognize the spike protein may be crucial for optimal disease control. Based on these analyses, EpiGen enables systematic investigation of antigen recognition patterns from single-cell TCR sequencing data.

3 Discussion

Precise identification of T-cell binding partners is crucial for understanding human adaptive immunity and developing targeted therapies, including immunotherapies and personalized vaccines. We introduced EpiGen, a large-scale transformer that generates potential epitope sequences from TCR data to enhance single-cell TCR sequencing analysis. To overcome the challenge of limited paired TCR-epitope data for model training, we developed a label propagation scheme, leveraging extensive unpaired data, complemented by the Antigen Category Filter algorithm to ensure biologically plausible antigen distributions.

Our comprehensive evaluation framework included novel approaches at multiple scales. At the repertoire level, we quantified the distributional characteristics of generated epitopes, to simulate real-world applications. This analysis was complemented by molecular dynamics simulations, providing physics-based binding affinity comparisons. Application of EpiGen to single-cell paired RNA and TCR sequencing datasets revealed important insights in both cancer and COVID-19 contexts. In cancer, phenotype-associated (PA) T cells - especially those clonally expanded in both tumor and normal adjacent tissue - showed enhanced cytotoxic marker and decreased exhaustion marker expressions compared to non-associated cells. These findings support the hypothesis of continuous peripheral replenishment of tumor-specific T cells[71]. In COVID-19, PA T cells from mild/moderate cases demonstrated increased clonal expansion with elevated cytotoxic markers compared to healthy controls, aligning with previously observed activated states[79,82,83]. In contrast, PA T cells in severe patients rather showed elevated naive/memory markers, which shows ineffective viral control in this group[78]. We also identified clonal expansion of $CD8^+$ T cells that recognize broader coronavirus antigens, which corroborate previous studies on $CD4^+$ T cells[84,85,91].

EpiGen's potential extends beyond the analyzed cancer types and COVID-19, offering promising applications in broader oncological contexts and viral infections. Its utility may encompass autoimmune conditions where $CD8^+$ T cells are pivotal, such as Type 1 Diabetes[94] and Multiple Sclerosis[95]. Furthermore, EpiGen could facilitate a deeper exploration of tumor microenvironments, potentially uncovering novel biomarkers to advance immunotherapy development.

Several limitations should be noted. EpiGen's analyses are most reliable in comparative analyses, such as comparing PA ratios across cell types, tracking immune responses, or assessing differences between patient groups. However, the absolute values of PA ratios require careful interpretation due to their dependence on the number of generated epitopes for each TCR, the completeness of the reference database, and TCR cross-reactivity. Although the current availability of TCR-epitope binding data bounds EpiGen performance, this limitation also highlights clear avenues for improvement. Future development efforts will incorporate the analysis of class II MHC-presented peptides, enabling the study of $CD4^+$ T cells and providing a more comprehensive understanding of the T cell repertoire.

To the best of our knowledge, EpiGen is the first tool available for epitope generation from TCR sequences, enabling the analysis of individual patient TCR repertoires. The model, its training data and strategy, as well as the evaluation framework, represent valuable resources for future advancements in this field. We envision EpiGen becoming an essential tool for analyzing TCR sequencing data and inspiring future efforts to develop advanced computational methods for TCR repertoire analysis.

4 Methods

Robust Affinity Predictor (RAP) training Training datasets for binding affinity predictors were compiled from four public sources: VDJdb, IEDB, PIRD, and McPAS-TCR. Data selection criteria included CDR3β lengths of 10-20 amino acids and epitope lengths of 8-12 amino acids. Samples containing non-standard amino acids were excluded. For VDJdb, only samples with vdjdb.score > 0 were considered. The resulting merged dataset comprised 116,057 TCR-epitope pairs, encompassing 98,460 unique TCRs and 1,141 unique epitopes. Detailed dataset split information was provided in **Supplementary Table 1**.

Robust Affinity Predictor, our binding affinity predictor for pseudo-labeling, was developed by modifying TABR-BERT with three architectural changes: implementing a Softmax layer in the head architecture, removing MHC-related architectures, and utilizing PyTorch's CrossEntropyLoss instead of Contrastive loss. For the second modification, we re-trained the BERT model[96] solely on epitope sequences, a process that took two days using two NVIDIA L40S GPUs.

A key challenge in training TCR-epitope binding predictors is the lack of confirmed non-binding pairs (negative pairs) in public datasets. To overcome this limitation, we developed Triple Negative Sampling (TNS), which generates diverse negative training examples through three complementary strategies. First, we pair known epitopes with TCRs from a large external pool (TCRNegSet, next section). Second, we generate negative samples by pairing

known TCRs with epitopes from a large external pool (EpiNegSet, next section). Third, we randomly pair TCRs and epitopes within the dataset, leveraging the assumption that random TCR-epitope pairs are unlikely to bind. This diversified negative sampling approach helps reduce potential biases arising from relying on any single sampling strategy. The final model combined the predictions of five independently trained models through ensemble averaging.

Datasets for pseudo-labeling Pseudo-labeling involves large-scale inference on randomly paired TCRs and epitopes using the Robust Affinity Predictor, selecting high-affinity samples for model training. We used the TCRdb dataset, which contained 19,701 TCR sequencing measurements as of May 2024, as the unpaired TCR sequence pool. TCRs with lengths between 10-20 amino acids and comprising only standard amino acids were selected, yielding 7,331,478 unique CDR3β sequences. These TCR CDR3β sequences were split into TCR-CandidateSet (6,831,478) for pseudo-labeling and TCRNegSet (500,000) for Triple Negative Sampling.

Epitope sequences were obtained from NetMHCPanv4.0 (Binding Affinity and Eluted Ligands datasets), MHCflurryv2.0 (S1-S5 datasets), and SysteMHC (per-MHC datasets from https://systemhc.sjtu.edu.cn/download). Epitopes of 8-12 amino acid length, containing only standard amino acids, were included, resulting in 21,801,187 unique sequences. When training EpiGenMHC, only MHC-epitope binding pairs were extracted, with the most likely MHC selected using the mhcflurry2.ba_best_allele column. Inhibitory Concentration 50% (IC50) units were converted to binary labels using the formula `lambda x: 1 - log(max(x, 0.1), 50000)`[97], with a threshold of 0.42 defining a hit. The epitope dataset was split into EpiCandidateSet (20,000,000) for pseudo-labeling and EpiNegSet (1,801,187) for Triple Negative Sampling.

Label Propagation algorithm The label propagation algorithm (**Algorithm 1**) generates a pseudo-labeled dataset of TCR-epitope pairs. Given sets of unpaired TCR sequences $\{t_i\}_{i=1}^{I}$ and epitope sequences $\{p_j\}_{j=1}^{J}$, the algorithm uses a binding affinity predictor function R (implemented as RAP) to estimate the binding affinity between TCRs and epitopes ($I = 6,831,478, J = 20,000,000$ were used). For each unpaired TCR t_i, the algorithm randomly samples $\beta = 10,000$ candidate epitopes from $\{p_j\}_{j=1}^{J}$. The binding affinity a is computed for each TCR-epitope pair (t_i, p) using R. Subsequently, the top $n_{\text{max_tcr}} = 32$ pairs with the highest binding affinities are retained for each TCR. To mitigate redundancy in the resulting dataset, a filtering step is applied. Epitopes that occur more than $n_{\text{max_epi}} = 100$ times in all pairs of TCR-epitopes are excluded. The value of $n_{\text{max_epi}}$ was determined based on the ratio of TCR to epitope observed in public datasets (specifically 116,057 epitopes to 1,141 TCR, resulting in a ratio of approximately 102). This process resulted in a pseudo-labeled dataset comprising $|\mathcal{D}| = 16,909,219$ TCR-epitope pairs. The algorithm took four days to run on ten NVIDIA L40S GPUs.

Antigen Category Filter The intermediate dataset $\mathcal{D}$ was biased towards Eukaryotic species, a consequence of the peptide collection methods used by NetMHCPanv4.0, MHCflurryv2.0, and SysteMHC. This bias likely reflects research priorities and funding rather than the biological distribution of antigens potentially recognized by $CD8^+$ T cells. To correct this dis-

Algorithm 1 Label Propagation of TCR-Epitope Binding Affinity

Require:

$\{t_i\}_{i=1}^{I}$: Set of unpaired TCR sequences
$\{p_j\}_{j=1}^{J}$: Set of unpaired epitope sequences
R: Binding affinity predictor function (RAP)
β: Number of epitopes to check for each TCR (10000)
$n_{\text{max_tcr}}$: Maximum number of epitopes per TCR (32)
$n_{\text{max_epi}}$: Maximum occurrences of an epitope (100)

Ensure: $\mathcal{D}$: A dictionary of TCR-epitope pairs with binding affinities

function LabelPropagation($\{t_i\}_{i=1}^{I}, \{p_j\}_{j=1}^{J}, R, \beta$)
    $\mathcal{D} \leftarrow \{\}$
    for $t_i \in \{t_i\}_{i=1}^{I}$ **do**
        $Q_i \leftarrow \text{RandomSample}(\{p_j\}_{j=1}^{J}, \beta)$
        $A_i \leftarrow \{\}$
        for $p \in Q_i$ **do**
            $a \leftarrow R(t_i, p)$
            $A_i \leftarrow A_i \cup (p, a)$
        end for
        $\mathcal{D}[t_i] \leftarrow \text{TopK}(A_i, n_{\text{max_tcr}})$
    end for
    $\mathcal{D} \leftarrow \text{FilterRedundancy}(D, n_{\text{max_epi}})$
    return $\mathcal{D}$
end function
function FilterRedundancy($\mathcal{D}, n_{\text{max_epi}}$)
    $C \leftarrow \text{CountEpitopeOccurrences}(\mathcal{D})$
    for $t_i, \text{pairs} \in \mathcal{D}.\text{items}()$ **do**
        $\mathcal{D}[t_i] \leftarrow (p, a) \in \text{pairs} : C[p] \leq n_{\text{max_epi}}$
    end for
    return $\mathcal{D}$
end function

Algorithm 2 Antigen Category Filter (ACF)

Require:

$\mathcal{D} = \{(t_l, p_l)\}_{l=1}^{L}$: Set of redundancy-removed pseudo-labeled TCR-epitope pairs

$\{(c_n, r_n)\}_{n=1}^{N}$: Set of antigen categories and their target ratios, where $\sum_{n=1}^{N} r_n = 1$, $N = 9$, and r_1 is the ratio for the pivot

Ensure: $\mathcal{C}$: Corpus, or TCR-epitope pairs with balanced antigen category

function AntigenCategoryFilter($\{(t_l, p_l)\}_{l=1}^{L}, \{(c_n, r_n)\}_{n=1}^{N}$)
  $\{(t_l, p_l, c_l)\}_{l=1}^{L} \leftarrow$ SearchCategory($\{(t_l, p_l)\}_{l=1}^{L}$)
  $M \leftarrow$ CountPivotCategory($\{(t_l, p_l, c_l)\}_{l=1}^{L}$)
  $\{c'_n\}_{n=1}^{N} \leftarrow \{M \cdot r_n / r_1\}_{n=1}^{N}$ // Target numbers to sample
  $\mathcal{C} \leftarrow \{\}$
  for $n \in 1, \ldots, N$ **do**
    $S_n \leftarrow (t_l, p_l) : (t_l, p_l, c_l) \in (t_l, p_l, c_l)_{l=1}^{L}$ and $c_l = c_n$
    $\mathcal{C} \leftarrow \mathcal{C} \cup$ RandomSample(S_n, c'_n)
  end for
  return $\mathcal{C}$
end function
function SearchCategory($\{(t_l, p_l)\}_{l=1}^{L}$)
  // Use blastp and NCBI database queries to determine species and categories
  // Return $\{(t_l, p_l, c_l)\}_{l=1}^{L}$ where c_l is the category for each pair
end function
function CountPivotCategory($(t_l, p_l, c_l)_{l=1}^{L}$)
  return $|(t_l, p_l, c_l) \in \{(t_l, p_l, c_l)\}_{l=1}^{L} : c_l =$ "Virus"$|$
end function

crepancy, we implemented the Antigen Category Filter (ACF) algorithm (**Algorithm 2**) to impose a biologically relevant epitope distribution. ACF takes as input a set of redundancy-removed pseudo-labeled TCR-epitope pairs $\{(t_l, p_l)\}_{l=1}^{L}$ and a set of antigen categories with their target ratios $\{(c_n, r_n)\}_{n=1}^{N}$.

To determine the target antigen ratios, we considered five immunological insights: (1) Viral Dominance: Studies indicate that a substantial proportion of $CD8^+$ T cells recognize viral antigens, with Masopust et al.[44] showing approximately 80% of splenic $CD8^+$ T cells recognize viral epitopes during peak infection. We set the proportion of viral antigens to be P(virus) $\geq$ 50%. (2) Limited Bacteria: Although certain bacterial species such as *Listeria monocytogenes* and *Mycobacterium tuberculosis* can elicit $CD8^+$ T cell responses through intracellular infection[98], their contribution is limited compared to viruses. We set bacterial antigens to P(bacteria) $\leq$ P(virus) $\times$ 0.2. (3) Endogenous Presence: Due to thymic negative selection[48], $CD8^+$ T cells that recognize self- or tumor antigens are less frequent than virus-specific T cells. Rizzuto et al.[49] confirmed the significantly lower frequency of self/tumor antigen-specific T cells than T cells specific for foreign antigens. We therefore constrained the self-antigen ratio in the range of 0.03-0.15 and the tumor antigen ratio in the range of 0.01-0.05. (4) Rare Fungi and Parasites: Although some fungi like *Histoplasma capsulatum*[99] can trigger $CD8^+$ T cell responses, their frequency is considerably lower, with only a few dozen fungal species causing regular human infections[100]. This led us to restrict their combined proportion to P(fungi + parasites) $\leq$ P(virus) $\times$ 0.1. (5) No Reported Pathogenic Archaea: Given the absence of documented archaeal pathogens causing human disease[101,102], we kept the proportion of archaeal antigens in our dataset very low (P(archaea)$\leq$0.01). The target proportions for each category were sampled from their respective ranges and normalized to ensure that their sum equaled one, while maintaining the defined biological constraints. More discussion of target ratio ranges was provided in **Supplementary Note 2**.

The Antigen Category Filter algorithm begins with a species identification process for each epitope, conducted using SwissProtDB through `blastp` queries (`-task blastp-short -evalue 20000 -max_target_steps 10`), accounting for the short epitope lengths. This step is encapsulated in the `SearchCategory` function. Subsequently, the NCBI accession numbers were utilized to query proteins and species using the command: `blastdbcmd -db ncbi-blast-2.15.0+/db/swissprot -entry_batch output.txt -outfmt "%a %t"`. Species lineage determination involved searching for TaxId from NCBI accession numbers and then querying lineage information from TaxId using `epost`, `esummary`, `xtract`, and `efetch` commands. The resulting XML files were parsed to categorize the species into categories. All viral epitopes were retained as pivot species (counted by the `CountPivotCategory` function).

EpiGen architecture and training EpiGen is a decoder-only transformer model specifically designed to generate epitope sequences while adhering to specific distributional constraints, including epitope diversity and biologically plausible antigen distributions. The model architecture is based on GPT-2, with amino acid sequences encoded using the BPETokenizer[103] from the Hugging Face[104] library. This tokenization method allows for

the representation of single amino acids or groups of amino acids as individual tokens, potentially capturing meaningful biological motifs. The Byte-Pair Encoding (BPE) algorithm iteratively merges the most frequent pairs of tokens, capturing the recurring subsequences as single tokens. Let $\mathcal{V}$ be the vocabulary of tokens, with $|\mathcal{V}|= 400$, which was found to efficiently encode all sequences with the optimal usage ratio (**Supplementary Note 5**). The BPETokenizer was trained using Corpus $\mathcal{C}$. For a TCR-epitope pair (t, p), the input sequence is tokenized as:

$$\mathbf{x} = [\text{BPE}(t); [\text{SEP}]; \text{BPE}(p); [\text{EOS}]] \tag{1}$$

where BPE$(\cdot)$ denotes the BPE tokenization function, ';' represents concatenation, [SEP] delineates the boundary between TCR and epitope sequences, and [EOS] marks the end of each sequence. The tokenized sequences were processed using positional embeddings, where position-specific vectors are added to the token embeddings to maintain sequence order information.

We adopted the GPT2-small architecture[27], a decoder-only transformer architecture introduced by Vaswani et al.[105]. The model consists of 12 transformer decoder layers, each containing a multi-head self-attention mechanism followed by a position-wise feedforward network. The self-attention mechanism in each layer has 12 attention heads, allowing the model to attend to different aspects of the input sequence simultaneously. Each head projects the input into query, key, and value spaces of dimension 64 (768/12, where 768 is the dimensionality of each token embedding), allowing the model to capture various types of sequential dependencies in TCRs. The position-wise feedforward network in each layer consists of two linear transformations with a Gaussian Error Linear Unit (GELU) activation function, expanding the intermediate representation to dimension 3,072 before projecting back to 768. This architecture, which contains 124 million parameters in total, was implemented using the HuggingFace and PyTorch[106] frameworks. The model defines a probability distribution $p_{\boldsymbol{\theta}}(\mathbf{x})$ over a sequence of tokens $\mathbf{x}$ of length n, which can be factorized as:

$$p_{\boldsymbol{\theta}}(\mathbf{x}) = \prod_{\tau=1}^{n} p_{\boldsymbol{\theta}}(\mathbf{x}_\tau | \mathbf{x}_{<\tau}) \tag{2}$$

where $\boldsymbol{\theta}$ represents the model parameters, $\mathbf{x}_\tau$ is the τ-th token in the sequence, and $\mathbf{x}_{<\tau}$ denotes all tokens before τ. This autoregressive formulation allows the model to generate epitope sequences token by token, conditioned on the input TCR sequence. The objective function for training is the negative log-likelihood:

$$\mathcal{L}(\boldsymbol{\theta}) = -\sum_{(t,p)\in\mathcal{C}} \log p_{\boldsymbol{\theta}}(\mathbf{x}). \tag{3}$$

Given the narrow length distribution of the TCR and epitope sequences compared to natural language paragraphs, each batch contained a single TCR-epitope pair. The AdamW optimizer[107] was used with parameters: initial learning rate ($\alpha = 1 \times 10^{-5}$), $\beta_1 = 0.9$,

$\beta_2 = 0.999$, $\epsilon = 1 \times 10^{-8}$, and weight decay ($\lambda = 0.01$). Training took four hours for EpiGen and four days for EpiGenNoACF using four NVIDIA L40S GPUs. Additional details on EpiGen training can be found in **Supplementary Note 5**.

Molecular Dynamics (MD) simulation MD simulation provides ways to evaluate the generated epitopes, which is orthogonal to measuring binding affinities using Robust Affinity Predictor, a deep learning-based predictor. After generating an epitope, the first step was to predict the 3D structure of the full TCR-pMHC complex. For this task, we employed TCRmodel2, which is based on AlphaFold2[65]. The model inputs comprised the full TCR alpha chain, the TCR beta chain, the epitope, and the full MHC sequence, with MHC alleles mapped to sequences referring to the IMGT/HLA Database[108]. The TCR alpha chain was fixed, while the TCR beta chain's CDR3β region was replaced with the input CDR3β sequence. Of the five PDB files generated by TCRmodel2, only `pdb_0` was used for subsequent analyses. After predicting the 3D structure, structure refinement and interface analysis were performed using Rosetta 3.14 (released March 7, 2024). The Rosetta `relax` application (`main/source/bin/relax.static.linuxgccrelease`) was executed with options `-relax:default_repeats 5 -nstruct 1` for structure relaxation. Then, interface analysis was performed using Rosetta's InterfaceAnalyzer (`main/source/bin/InterfaceAnalyzer.static.linuxgccrelease`) to examine protein-protein interface properties.

Wu et al. dataset preprocessing The dataset from Wu et al.[71] was obtained from Gene Expression Omnibus (GEO) with access number GSE139555, containing clustering, cell type annotation, and TCR contig annotation information. We focused on cells from clusters 8.1-Teff, 8.2-Tem, 8.3a-Trm, 8.3b-Trm, epiand 8.3c-Trm, re-labeled as Teff, Tem, Trm-a, Trm-b, and Trm-c for brevity. The dataset comprised samples from 14 donors in four types of cancer (lung, renal, endometrial, and colorectal), collected from tumor tissue, normal adjacent tissue (NAT), and blood whenever available. The preprocessed data, which contain highly variable genes, UMAP coordinates, cell subtypes, and clonotype information, were initially loaded. To integrate the RNA and TCR sequencing data, we used the scirpy package[109]. We read the TCR data from files with the `contig_annotations.csv` suffix using `scirpy`'s `ir.io.read_10_vdj()` function. The resulting information was stored in a MultiModalData (MuData) object, combining both RNA and TCR data. For TCR analysis, we performed quality control using `scirpy`'s `ir.pp.index_chains()` and `ir.tl.chain_qc()` functions. We retained cells with chain pairings classified as 'single pair', 'orphan VDJ', 'extra VJ', or 'extra VDJ'. In cases of 'extra VDJ', we selected the first entry. Only productive TRB chains were included for further analysis, as non-productive chains are excluded by `scirpy`. For each cell, we extracted the TRB locus, amino acid junction (CDR3_aa), and nucleotide junction (CDR3_nt) sequences. This information was then merged with the gene expression data based on cell identifiers, resulting in a dataset of 36,986 cells with matched gene expression and TCR information. This dataset contained 9,166 unique CDR3_aa sequences and 9,284 unique CDR3_nt sequences. To analyze the expression levels of genes of interest, we utilized the raw dataset of `barcodes.tsv`, `genes.tsv`, and `matrix.mtx` files, which were loaded using `scanpy`'s[110] `sc.read_10x_mtx()` function. We obtained the curated list of genes associated with $CD8^+$ T cells from Wu et al., including exhaustion markers (e.g.,

PDCD1, *CTLA4*, *LAG3*), activation and proliferation markers (e.g., *CD69*, *IL2RA*, *MKI67*), TCR pathway-related genes (e.g., *ZAP70*, *LAT*, *LCK*), cytokines (e.g., *IFNG*, *TNF*), and various other markers related to T cell function and differentiation. The data were normalized to a total count of 10^4 per cell and log-transformed. While the clones were defined based on CDR3_nt, EpiGen used CDR3_aa to generate epitope sequences. These epitopes were then queried against a combined database derived from the Immune Epitope Database (IEDB)[36] and The Cancer Immunome Atlas (TCIA)[111], focusing on cancer-related linear epitopes restricted by MHC Class I. The epitopes found in these databases were classified as Phenotype-Associated (PA). Finally, the site patterns of the TCRs were annotated on the basis of their presence in different tissue sites. Statistical analyses, including comparisons between groups, were performed using two-sided Wilcoxon rank-sum test (`scanpy`[110]). Additional details on processing Wu et al. dataset can be found in **Supplementary Note 6**.

Su et al. dataset preprocessing For the analysis of COVID-19-related T-cell responses, we utilized the dataset from Su et al.[78], which comprises paired single-cell RNA and TCR sequencing data from 139 donors. We processed the data by first combining all the files with the format `heathlab_dc_9_17_pbmc_gex_library_XX_X.txt` to create a comprehensive `AnnData` object indexed by cell barcodes. TCR information was extracted from files formatted as `heathlab_dc_9_17_pbmc_cd8_tcr_library_XX_X.txt` and used to filter the `AnnData` object, retaining only cells with associated TCR data. The resulting dataset contained 50,284 unique cells, containing 26,170 unique CDR3 amino acid sequences and 26,621 unique CDR3 nucleotide sequences. We annotated the data with patient demographics and WHO Ordinal Scale scores, mapping the latter to four categories: healthy (0), mild (1 or 2), moderate (3 or 4), and severe (5, 6, or 7). For cell type annotation, we performed standard single-cell RNA sequencing analysis, including normalization, log transformation, selection of 1000 highly variable genes supplemented with the signature genes of $CD8^+$ T cells, PCA dimensionality reduction (50 components), Leiden clustering (resolution 1.0), and UMAP visualization. This process identified seven major clusters, which we grouped into four subtypes based on selectively high expression of marker genes: naive (*TCF7*, *LEF1*, *SELL*, *CCR7*), memory (*GZMK*), effector (*NKG7*, *CCL4*, *CST7*, *PRF1*, *GZMA*, *GZMB*), and proliferating (proliferation markers such as *MKI67*, *TYMS*). To identify COVID-19-associated epitopes, we constructed a database using IEDB, querying for linear sequence epitopes from SARS-CoV-2, with positive assays, MHC Class I restriction, and association of COVID-19 disease, resulting in 1,357 unique epitopes. We then used EpiGen to generate epitopes based on the CDR3 amino acid sequences. The matches were defined by a Levenshtein distance ≤ 1 with the first match selected in the cases of multiple matches. This preprocessing pipeline allowed us to integrate transcriptomic, clonotypic, and epitope-specific information. Additional details on the processing of the Su et al. dataset can be found in **Supplementary Note 7**.

References

1. Chaplin, D. D. Overview of the immune response. *J Allergy Clin Immunol* **125**, S3–23 (2010).

2. Andersen, M. H., Schrama, D., Thor Straten, P. & Becker, J. C. Cytotoxic T cells. *J Invest Dermatol* **126**, 32–41 (2006).

3. Tonegawa, S. Somatic generation of antibody diversity. *Nature* **302**, 575–581 (1983).

4. Parham, P. & Ohta, T. Population biology of antigen presentation by mhc class i molecules. *Science* **272**, 67–74 (1996).

5. Shannon, C. E. A mathematical theory of communication. *The Bell System Technical Journal* **27**, 379–423 (1948).

6. Simpson, E. H. Measurement of diversity. *Nature* **163**, 688–688 (1949).

7. Rényi, A. On measures of entropy and information. In *Proceedings of the Fourth Berkeley Symposium on Mathematical Statistics and Probability, Volume 1: Contributions to the Theory of Statistics*, 547–561 (University of California Press, Berkeley, California, 1961).

8. Janarthanam, R. *et al.* Bulk t-cell receptor sequencing confirms clonality in pediatric eosinophilic esophagitis and identifies a food-specific repertoire. *Allergy* **78**, 2487–2496 (2023).

9. Vujović, M., Marcatili, P., Chain, B., Kaplinsky, J. & Andresen, T. L. Signatures of T cell immunity revealed using sequence similarity with TCRDivER algorithm. *Communications Biology* **6**, 357 (2023).

10. Huang, H., Wang, C., Rubelt, F., Scriba, T. J. & Davis, M. M. Analyzing the mycobacterium tuberculosis immune response by t-cell receptor clustering with GLIPH2 and genome-wide antigen screening. *Nature Biotechnology* **38**, 1194–1202 (2020).

11. Mayer-Blackwell, K. *et al.* Tcr meta-clonotypes for biomarker discovery with *tcrdist3* enabled identification of public, hla-restricted clusters of sars-cov-2 tcrs. *eLife* **10**, e68605 (2021).

12. Sidhom, J.-W., Larman, H. B., Pardoll, D. M. & Baras, A. S. DeepTCR is a deep learning framework for revealing sequence concepts within t-cell repertoires. *Nature Communications* **12**, 1605 (2021).

13. Zhang, H., Zhan, X. & Li, B. GIANA allows computationally-efficient TCR clustering and multi-disease repertoire classification by isometric transformation. *Nature Communications* **12**, 4699 (2021).

14. Lu, T. *et al.* Deep learning-based prediction of the T cell receptor–antigen binding specificity. *Nature Machine Intelligence* **3**, 864–875 (2021).

15. Gao, Y. *et al.* Pan-Peptide meta learning for t-cell receptor–antigen binding recognition. *Nature Machine Intelligence* **5**, 236–249 (2023).

16. Chronister, W. D. *et al.* TCRMatch: Predicting T-Cell receptor specificity based on sequence similarity to previously characterized receptors. *Front Immunol* **12**, 640725 (2021).

17. Weber, A., Born, J. & Rodriguez Martínez, M. TITAN: T-cell receptor specificity prediction with bimodal attention networks. *Bioinformatics* **37**, i237–i244 (2021).

18. Jokinen, E., Huuhtanen, J., Mustjoki, S., Heinonen, M. & Lähdesmäki, H. Predicting recognition between T cell receptors and epitopes with TCRGP. *PLoS Comput Biol* **17**, e1008814 (2021).

19. Montemurro, A. *et al.* NetTCR-2.0 enables accurate prediction of TCR-peptide binding by using paired TCRα and β sequence data. *Communications Biology* **4**, 1060 (2021).

20. Zhang, W. *et al.* A framework for highly multiplexed dextramer mapping and prediction of t cell receptor sequences to antigen specificity. *Science Advances* **7**, eabf5835 (2021).

21. Tong, Y. *et al.* SETE: Sequence-based ensemble learning approach for TCR epitope binding prediction. *Comput Biol Chem* **87**, 107281 (2020).

22. Springer, I., Besser, H., Tickotsky-Moskovitz, N., Dvorkin, S. & Louzoun, Y. Prediction of specific tcr-peptide binding from large dictionaries of tcr-peptide pairs. *Frontiers in Immunology* **11** (2020).

23. Zhang, J., Ma, W. & Yao, H. Accurate TCR-pMHC interaction prediction using a BERT-based transfer learning method. *Briefings in Bioinformatics* **25**, bbad436 (2023).

24. Peng, X. *et al.* Characterizing the interaction conformation between t-cell receptors and epitopes with deep learning. *Nature Machine Intelligence* **5**, 395–407 (2023).

25. Cai, M., Bang, S., Zhang, P. & Lee, H. ATM-TCR: TCR-Epitope binding affinity prediction using a Multi-Head Self-Attention model. *Front Immunol* **13**, 893247 (2022).

26. Moris, P. *et al.* Current challenges for unseen-epitope TCR interaction prediction and a new perspective derived from image classification. *Briefings in Bioinformatics* **22**, bbaa318 (2020).

27. Radford, A. *et al.* Language models are unsupervised multitask learners (2019).

28. Lewis, M. *et al.* BART: Denoising sequence-to-sequence pre-training for natural language generation, translation, and comprehension. In Jurafsky, D., Chai, J., Schluter, N. & Tetreault, J. (eds.) *Proceedings of the 58th Annual Meeting of the Association for Computational Linguistics*, 7871–7880 (Association for Computational Linguistics, Online, 2020).

29. Raffel, C. *et al.* Exploring the limits of transfer learning with a unified text-to-text transformer. *J. Mach. Learn. Res.* **21** (2020).

30. Hudson, D., Fernandes, R. A., Basham, M., Ogg, G. & Koohy, H. Can we predict T cell specificity with digital biology and machine learning? *Nature Reviews Immunology* **23**, 511–521 (2023).

31. Grifoni, A. *et al.* Targets of T cell responses to SARS-CoV-2 coronavirus in humans with COVID-19 disease and unexposed individuals. *Cell* **181**, 1489–1501.e15 (2020).

32. Ferruz, N., Schmidt, S. & Höcker, B. ProtGPT2 is a deep unsupervised language model for protein design. *Nature Communications* **13**, 4348 (2022).

33. Nijkamp, E., Ruffolo, J. A., Weinstein, E. N., Naik, N. & Madani, A. ProGen2: Exploring the boundaries of protein language models. *Cell Systems* **14**, 968–978.e3 (2023).

34. Lee, D.-H. Pseudo-label : The simple and efficient semi-supervised learning method for deep neural networks. *ICML 2013 Workshop : Challenges in Representation Learning (WREPL)* (2013).

35. Shugay, M. *et al.* VDJdb: a curated database of t-cell receptor sequences with known antigen specificity. *Nucleic Acids Res* **46**, D419–D427 (2018).

36. Vita, R. *et al.* The immune epitope database (iedb): 2018 update. *Nucleic Acids Research* **47** (2019).

37. Zhang, W. *et al.* PIRD: Pan immune repertoire database. *Bioinformatics* **36**, 897–903 (2019).

38. Tickotsky, N., Sagiv, T., Prilusky, J., Shifrut, E. & Friedman, N. McPAS-TCR: a manually curated catalogue of pathology-associated T cell receptor sequences. *Bioinformatics* **33**, 2924–2929 (2017).

39. Chen, S.-Y., Yue, T., Lei, Q. & Guo, A.-Y. TCRdb: a comprehensive database for t-cell receptor sequences with powerful search function. *Nucleic Acids Res* **49**, D468–D474 (2021).

40. Jurtz, V. *et al.* NetMHCpan-4.0: Improved Peptide-MHC class I interaction predictions integrating eluted ligand and peptide binding affinity data. *J Immunol* **199**, 3360–3368 (2017).

41. O'Donnell, T. J., Rubinsteyn, A. & Laserson, U. Mhcflurry 2.0: Improved pan-allele prediction of mhc class i-presented peptides by incorporating antigen processing. *Cell Systems* **11**, 42–48.e7 (2020).

42. Huang, X. *et al.* The SysteMHC Atlas v2.0, an updated resource for mass spectrometry-based immunopeptidomics. *Nucleic Acids Research* **52**, D1062–D1071 (2023).

43. Neefjes, J., Jongsma, M. L. M., Paul, P. & Bakke, O. Towards a systems understanding of MHC class I and MHC class II antigen presentation. *Nature Reviews Immunology* **11**, 823–836 (2011).

44. Masopust, D., Murali-Krishna, K. & Ahmed, R. Quantitating the magnitude of the lymphocytic choriomeningitis virus-specific cd8 t-cell response: It is even bigger than we thought. *Journal of Virology* **81**, 2002–2011 (2007).

45. Moutaftsi, M. *et al.* A consensus epitope prediction approach identifies the breadth of murine TCD8+-cell responses to vaccinia virus. *Nature Biotechnology* **24**, 817–819 (2006).

46. Addo, M. M. *et al.* Comprehensive epitope analysis of human immunodeficiency virus type 1 (HIV-1)-specific t-cell responses directed against the entire expressed HIV-1 genome demonstrate broadly directed responses, but no correlation to viral load. *J Virol* **77**, 2081–2092 (2003).

47. Pittet, M. J. *et al.* High frequencies of naive Melan-A/MART-1-specific CD8(+) T cells in a large proportion of human histocompatibility leukocyte antigen (HLA)-A2 individuals. *J Exp Med* **190**, 705–715 (1999).

48. Kenison, J. E., Stevens, N. A. & Quintana, F. J. Therapeutic induction of antigen-specific immune tolerance. *Nature Reviews Immunology* **24**, 338–357 (2024).

49. Rizzuto, G. A. *et al.* Self-antigen-specific CD8+ T cell precursor frequency determines the quality of the antitumor immune response. *J Exp Med* **206**, 849–866 (2009).

50. Nelson, C. E. *et al.* Robust iterative stimulation with Self-Antigens overcomes CD8(+) T cell tolerance to self- and tumor antigens. *Cell Rep* **28**, 3092–3104.e5 (2019).

51. Fan, A., Lewis, M. & Dauphin, Y. Hierarchical neural story generation. In Gurevych, I. & Miyao, Y. (eds.) *Proceedings of the 56th Annual Meeting of the Association for Computational Linguistics (Volume 1: Long Papers)*, 889–898 (Association for Computational Linguistics, Melbourne, Australia, 2018).

52. Holtzman, A., Buys, J., Du, L., Forbes, M. & Choi, Y. The curious case of neural text degeneration. In *ICLR* (OpenReview.net, 2020).

53. Glanville, J. *et al.* Identifying specificity groups in the T cell receptor repertoire. *Nature* **547**, 94–98 (2017).

54. Nolan, S. *et al.* A large-scale database of t-cell receptor beta (TCRβ) sequences and binding associations from natural and synthetic exposure to SARS-CoV-2 (2020).

55. 10x Genomics. A new way of exploring immunity: Linking highly multiplexed antigen recognition to immune repertoire and phenotype. Application Note, 10x Genomics (2022).

56. Trolle, T. *et al.* The length distribution of class i–restricted t cell epitopes is determined by both peptide supply and mhc allele–specific binding preference. *The Journal of Immunology* **196**, 1480–1487 (2016).

57. Wilkins, M. R. *et al.* Protein identification and analysis tools in the ExPASy server. *Methods Mol Biol* **112**, 531–552 (1999).

58. Camacho, C. *et al.* BLAST+: architecture and applications. *BMC Bioinformatics* **10**, 421 (2009).

59. Madani, A. *et al.* Large language models generate functional protein sequences across diverse families. *Nature Biotechnology* **41**, 1099–1106 (2023).

60. Ashburner, M. *et al.* Gene ontology: tool for the unification of biology. *Nature Genetics* **25**, 25–29 (2000).

61. McCammon, J. A., Gelin, B. R. & Karplus, M. Dynamics of folded proteins. *Nature* **267**, 585–590 (1977).

62. Stranges, P. B. & Kuhlman, B. A comparison of successful and failed protein interface designs highlights the challenges of designing buried hydrogen bonds. *Protein Sci* **22**, 74–82 (2012).

63. Leaver-Fay, A. *et al.* ROSETTA3: an object-oriented software suite for the simulation and design of macromolecules. *Methods Enzymol* **487**, 545–574 (2011).

64. Yin, R. *et al.* TCRmodel2: high-resolution modeling of T cell receptor recognition using deep learning. *Nucleic Acids Res* **51**, W569–W576 (2023).

65. Jumper, J. *et al.* Highly accurate protein structure prediction with AlphaFold. *Nature* **596**, 583–589 (2021).

66. Gonzalez-Galarza, F. F., Christmas, S., Middleton, D. & Jones, A. R. Allele frequency net: a database and online repository for immune gene frequencies in worldwide populations. *Nucleic Acids Res* **39**, D913–9 (2010).

67. Sehnal, D. *et al.* Mol* Viewer: modern web app for 3D visualization and analysis of large biomolecular structures. *Nucleic Acids Research* **49**, W431–W437 (2021).

68. Alford, R. F. *et al.* The rosetta All-Atom energy function for macromolecular modeling and design. *J Chem Theory Comput* **13**, 3031–3048 (2017).

69. Dill, K. A. Dominant forces in protein folding. *Biochemistry* **29**, 7133–7155 (1990).

70. Fridman, W. H., Pagès, F., Sautès-Fridman, C. & Galon, J. The immune contexture in human tumours: impact on clinical outcome. *Nature Reviews Cancer* **12**, 298–306 (2012).

71. Wu, T. D. *et al.* Peripheral T cell expansion predicts tumour infiltration and clinical response. *Nature* **579**, 274–278 (2020).

72. Zhang, N. & Bevan, M. J. CD8(+) T cells: foot soldiers of the immune system. *Immunity* **35**, 161–168 (2011).

73. Yost, K. E. *et al.* Clonal replacement of tumor-specific T cells following PD-1 blockade. *Nature Medicine* **25**, 1251–1259 (2019).

74. Zhang, L. *et al.* Lineage tracking reveals dynamic relationships of T cells in colorectal cancer. *Nature* **564**, 268–272 (2018).

75. Simoni, Y. *et al.* Bystander CD8+ T cells are abundant and phenotypically distinct in human tumour infiltrates. *Nature* **557**, 575–579 (2018).

76. Waldman, A. D., Fritz, J. M. & Lenardo, M. J. A guide to cancer immunotherapy: from T cell basic science to clinical practice. *Nature Reviews Immunology* **20**, 651–668 (2020).

77. Esfahani, K. *et al.* A review of cancer immunotherapy: From the past, to the present, to the future. *Current Oncology* **27**, 87–97 (2020).

78. Su, Y. *et al.* Multi-omics resolves a sharp disease-state shift between mild and moderate covid-19. *Cell* **183**, 1479–1495.e20 (2020).

79. Rydyznski Moderbacher, C. *et al.* Antigen-Specific adaptive immunity to SARS-CoV-2 in acute COVID-19 and associations with age and disease severity. *Cell* **183**, 996–1012.e19 (2020).

80. Chen, Z. & John Wherry, E. T cell responses in patients with COVID-19. *Nature Reviews Immunology* **20**, 529–536 (2020).

81. Henikoff, S. & Henikoff, J. G. Amino acid substitution matrices from protein blocks. *Proc Natl Acad Sci U S A* **89**, 10915–10919 (1992).

82. Sekine, T. *et al.* Robust T cell immunity in convalescent individuals with asymptomatic or mild COVID-19. *Cell* **183**, 158–168.e14 (2020).

83. Stephenson, E. *et al.* Single-cell multi-omics analysis of the immune response in COVID-19. *Nature Medicine* **27**, 904–916 (2021).

84. Nelde, A. *et al.* SARS-CoV-2-derived peptides define heterologous and COVID-19-induced T cell recognition. *Nature Immunology* **22**, 74–85 (2021).

85. Mateus, J. *et al.* Selective and cross-reactive sars-cov-2 t cell epitopes in unexposed humans. *Science* **370**, 89–94 (2020).

86. Moss, P. The T cell immune response against SARS-CoV-2. *Nature Immunology* **23**, 186–193 (2022).

87. Kared, H. *et al.* Sars-cov-2–specific cd8+ t cell responses in convalescent covid-19 individuals. *The Journal of Clinical Investigation* **131** (2021).

88. Gangaev, A. *et al.* Identification and characterization of a SARS-CoV-2 specific CD8+ T cell response with immunodominant features. *Nature Communications* **12**, 2593 (2021).

89. Zheng, H.-Y. *et al.* Elevated exhaustion levels and reduced functional diversity of T cells in peripheral blood may predict severe progression in COVID-19 patients. *Cellular & Molecular Immunology* **17**, 541–543 (2020).

90. Functional exhaustion of antiviral lymphocytes in COVID-19 patients. *Cellular & Molecular Immunology* **17**, 533–535 (2020).

91. Braun, J. *et al.* SARS-CoV-2-reactive T cells in healthy donors and patients with COVID-19. *Nature* **587**, 270–274 (2020).

92. Peng, Y. *et al.* Broad and strong memory CD4+ and CD8+ T cells induced by SARS-CoV-2 in UK convalescent individuals following COVID-19. *Nature Immunology* **21**, 1336–1345 (2020).

93. Early induction of functional SARS-CoV-2-specific T cells associates with rapid viral clearance and mild disease in COVID-19 patients. *Cell Reports* **34** (2021).

94. Bluestone, J. A., Herold, K. & Eisenbarth, G. Genetics, pathogenesis and clinical interventions in type 1 diabetes. *Nature* **464**, 1293–1300 (2010).

95. Huseby, E. S., Huseby, P. G., Shah, S., Smith, R. & Stadinski, B. D. Pathogenic CD8 T cells in multiple sclerosis and its experimental models. *Frontiers in Immunology* **3** (2012).

96. Devlin, J., Chang, M.-W., Lee, K. & Toutanova, K. Bert: Pre-training of deep bidirectional transformers for language understanding. In *North American Chapter of the Association for Computational Linguistics* (2019).

97. Nielsen, M. *et al.* NetMHCpan, a method for quantitative predictions of peptide binding to any HLA-A and -B locus protein of known sequence. *PLoS One* **2**, e796 (2007).

98. Shepherd, F. R. & McLaren, J. E. T cell immunity to bacterial pathogens: Mechanisms of immune control and bacterial evasion. *Int J Mol Sci* **21** (2020).

99. Mittal, J., Ponce, M. G., Gendlina, I. & Nosanchuk, J. D. Histoplasma capsulatum: Mechanisms for pathogenesis. *Curr Top Microbiol Immunol* **422**, 157–191 (2019).

100. Stuckey Peter V. & Santiago-Tirado Felipe H. Fungal mechanisms of intracellular survival: what can we learn from bacterial pathogens? *Infection and Immunity* **91**, e00434–22 (2023).

101. Cavicchioli, R., Curmi, P. M., Saunders, N. & Thomas, T. Pathogenic archaea: do they exist? *BioEssays* **25**, 1119–1128 (2003).

102. Gill, E. E. & Brinkman, F. S. L. The proportional lack of archaeal pathogens: Do viruses/phages hold the key? *BioEssays* **33**, 248–254 (2011).

103. Sennrich, R., Haddow, B. & Birch, A. Neural machine translation of rare words with subword units. In Erk, K. & Smith, N. A. (eds.) *Proceedings of the 54th Annual Meeting of the Association for Computational Linguistics (Volume 1: Long Papers)*, 1715–1725 (Association for Computational Linguistics, Berlin, Germany, 2016).

104. Wolf, T. *et al.* Transformers: State-of-the-art natural language processing. In Liu, Q. & Schlangen, D. (eds.) *Proceedings of the 2020 Conference on Empirical Methods in Natural Language Processing: System Demonstrations*, 38–45 (Association for Computational Linguistics, Online, 2020).

105. Vaswani, A. *et al.* Attention is all you need. In Guyon, I. *et al.* (eds.) *Advances in Neural Information Processing Systems*, vol. 30 (Curran Associates, Inc., 2017).

106. Paszke, A. *et al. PyTorch: an imperative style, high-performance deep learning library* (Curran Associates Inc., Red Hook, NY, USA, 2019).

107. Loshchilov, I. & Hutter, F. Decoupled weight decay regularization. In *International Conference on Learning Representations* (2017).

108. Barker, D. J. *et al.* The IPD-IMGT/HLA Database. *Nucleic Acids Research* **51**, D1053–D1060 (2022).

109. Sturm, G. *et al.* Scirpy: a scanpy extension for analyzing single-cell t-cell receptor-sequencing data. *Bioinformatics* **36**, 4817–4818 (2020).

110. Wolf, F. A., Angerer, P. & Theis, F. J. SCANPY: large-scale single-cell gene expression data analysis. *Genome Biology* **19**, 15 (2018).

111. Charoentong, P. *et al.* Pan-cancer immunogenomic analyses reveal genotype-immunophenotype relationships and predictors of response to checkpoint blockade. *Cell Reports* **18**, 248–262 (2017).

Acknowledgements

This work was supported by a Discovery grant from the Natural Sciences and Engineering Research Council (NSERC) of Canada, and a department startup fund from the University of British Columbia (to J.D.). J.D. is a Canada Research Chair and is supported by the Canadian Institutes of Health Research through the Canada Research Chair Program. The computational resource is partially supported by the Canada Foundation for Innovation & John. R. Evans Leader Fund (to J.D.). This research was supported in part through the computational resources and services provided by Advanced Research Computing at the University of British Columbia.

Author's contributions

M.M. developed and implemented the model, conducted experiments, and prepared the manuscript with input from J.D. W.T. and C.V. assisted with data analysis. J.D. supervised the project. All authors reviewed and approved the manuscript.

Competing financial interests

The authors declare no competing interests.

5 Extended Data Figure

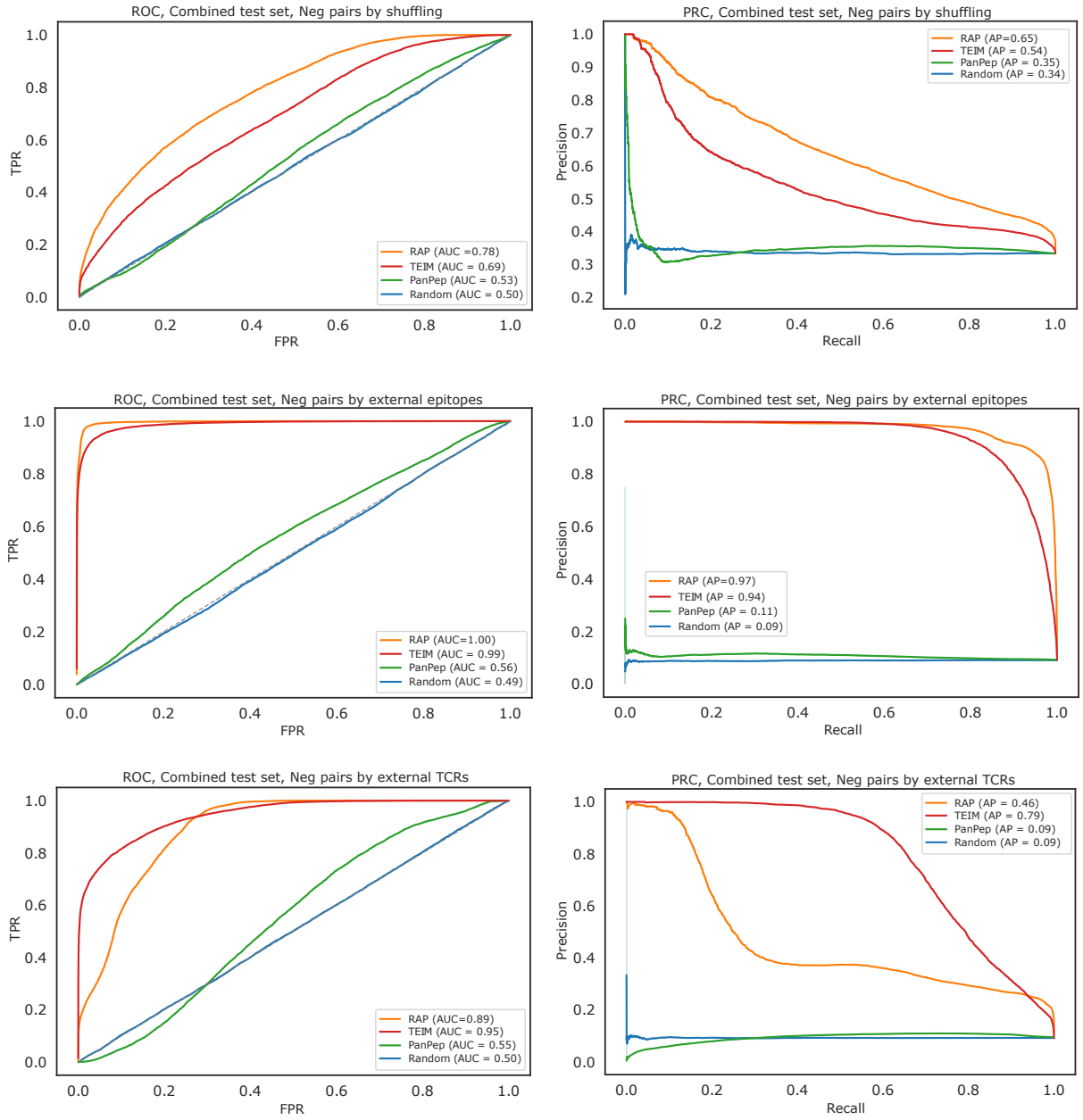

Extended Data Fig. 1: **Receiver Operating Curves (ROC) and Precision-Recall Curves (PRC) of Robust Affinity Predictor (RAP) and other competing binding affinity predictors.** ROC and PRC of the binding affinity predictors on the combined public test set that comes from four sources: VDJdb, IEDB, PIRD, and McPAS-TCR. Three scenarios of negative sample generation were considered: randomly pairing TCR and epitope in the test set (top), pairing the TCRs with external epitopes (middle), and pairing the epitopes with external TCRs (bottom). Four models were compared: Robust Affinity Predictor (RAP), TEIM, PanPep, and Random. AUC or AP values are denoted in the legends next to the model names.

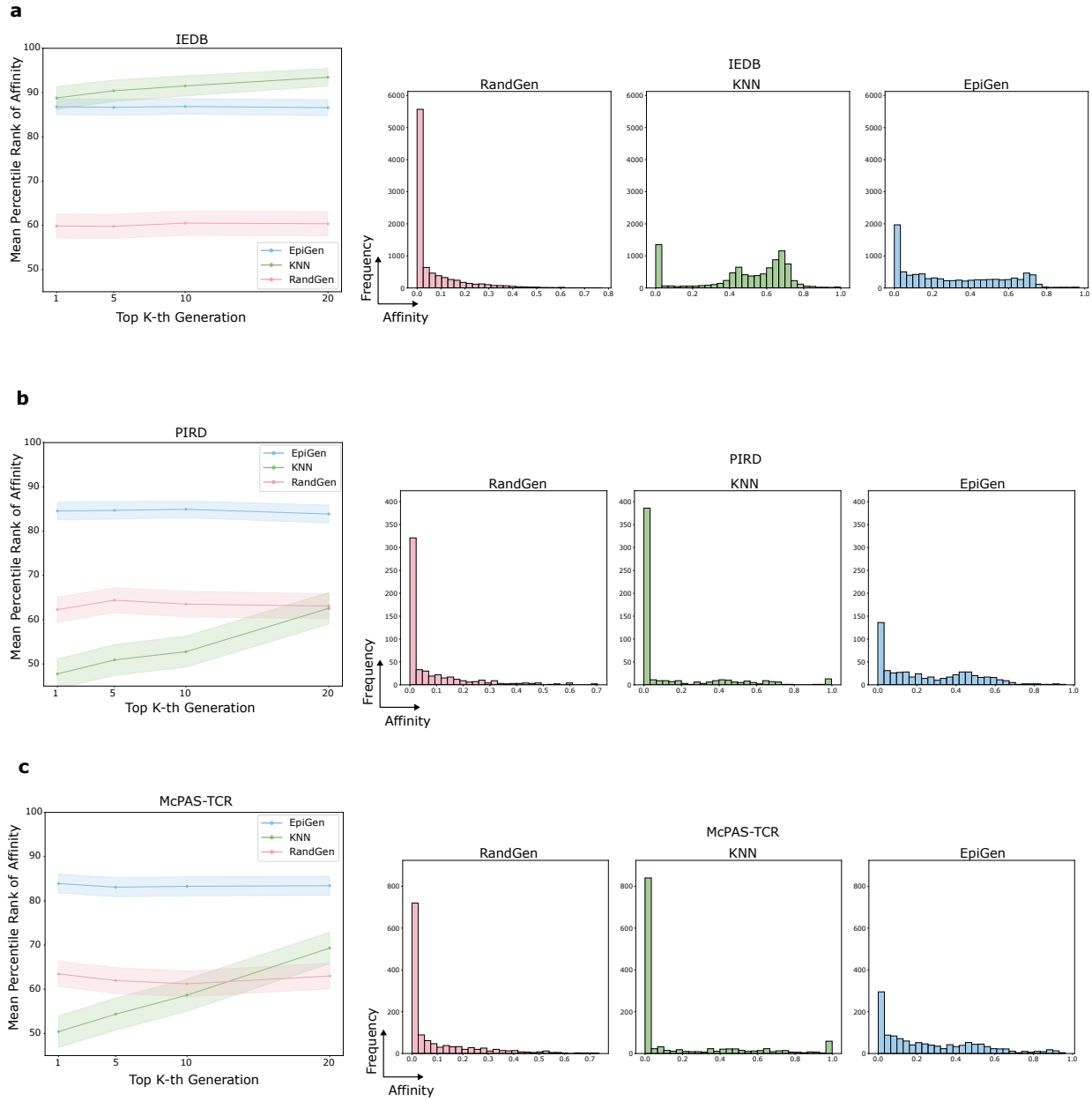

Extended Data Fig. 2: **Validation of high binding affinities between EpiGen-generated epitopes and input TCRs.** **a–c.** The validation results by the test sets: IEDB, PIRD, and McPAS-TCR. The plots show the mean percentile rank of the binding affinities between the top K generated epitopes and TCRs (left) and the predicted binding affinity distributions (right). Three methods were were compared: RandGen, KNN, and EpiGen. Higher binding affinity values are favored.

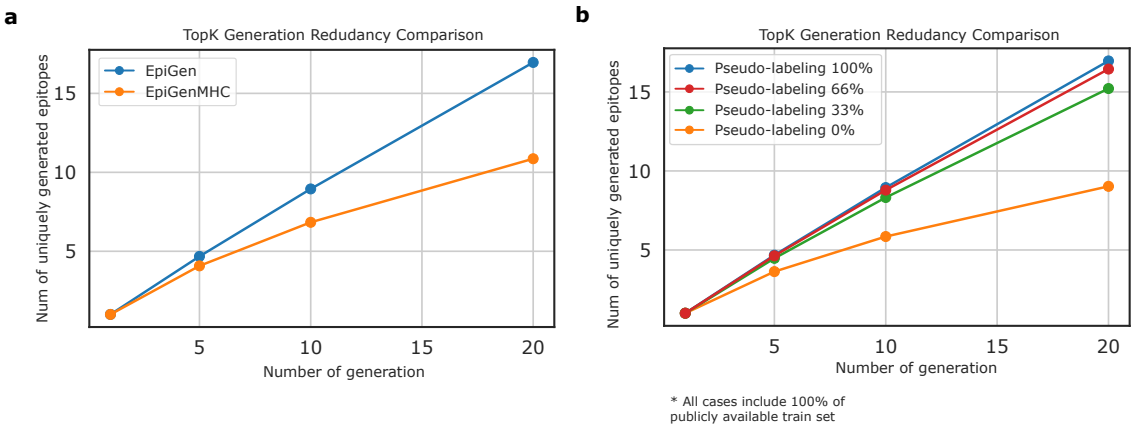

Extended Data Fig. 3: Comparison of redundancy in multiple generations on repertoire-level dataset. **a.** Plot showing the average number of uniquely generated epitopes (y-axis) by the number of generation attempt for each TCR (x-axis). The top generations may produce the same epitope sequences, leading to redundancy. The plot highlights the redundancy of EpiGenMHC. The dataset was the 10x dataset. **b.** Plot showing the average number of uniquely generated epitopes (y-axis) by the number of generation attempt for each TCR (x-axis). The plot compares four models trained using different amount of pseudo-labeled dataset from 0%, 33%, 66% to 100%. The dataset was the 10x dataset.

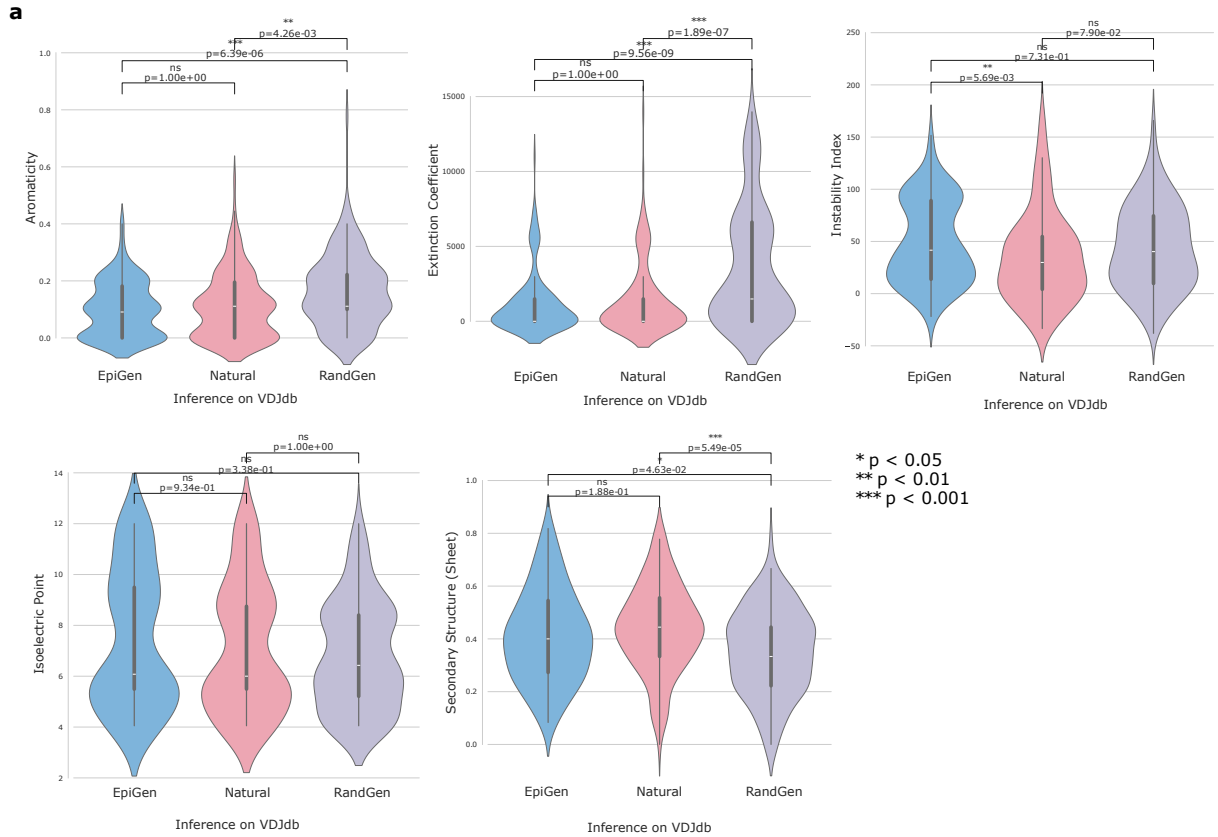
a
Aromaticity
Extinction Coefficient
Instability Index
Isoelectric Point
Secondary Structure (Sheet)
EpiGen
Natural
RandGen
Inference on VDJdb
ns
p=1.00e+00
**
p=4.26e-03
***
p=6.39e-06
***
p=1.89e-07
***
p=9.56e-09
ns
p=7.90e-02
ns
p=7.31e-01
**
p=5.69e-03
ns
p=3.38e-01
ns
p=9.34e-01
***
p=5.49e-05
***
p=4.63e-02
ns
p=1.88e-01
* p < 0.05
** p < 0.01
*** p < 0.001

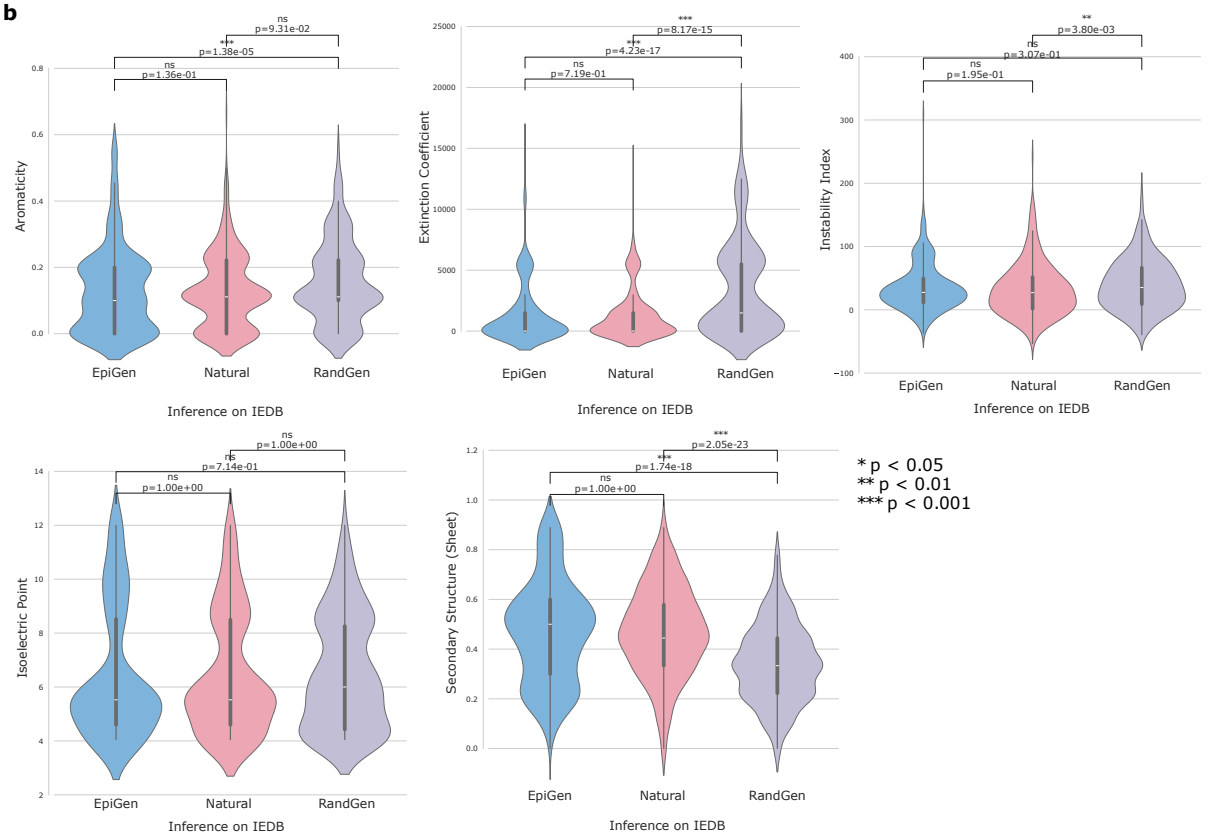
b
Aromaticity
Extinction Coefficient
Instability Index
Isoelectric Point
Secondary Structure (Sheet)
EpiGen
Natural
RandGen
Inference on IEDB
ns
p=9.31e-02
***
p=1.38e-05
ns
p=1.36e-01
***
p=8.17e-15
***
p=4.23e-17
ns
p=7.19e-01
**
p=3.80e-03
ns
p=3.07e-01
ns
p=1.95e-01
ns
p=1.00e+00
ns
p=7.14e-01
ns
p=1.00e+00
***
p=2.05e-23
**
p=1.74e-18
ns
p=1.00e+00
* p < 0.05
** p < 0.01
*** p < 0.001

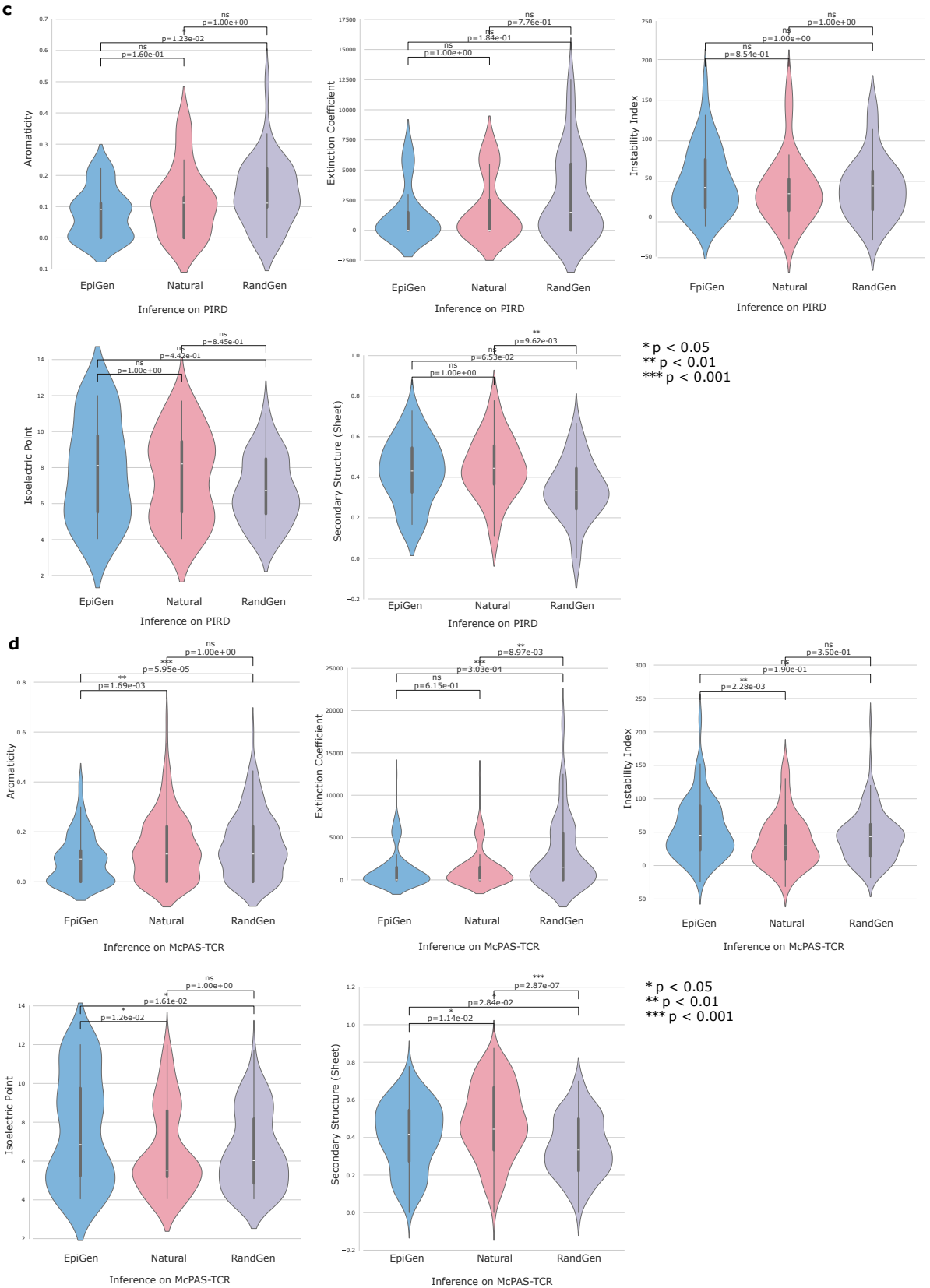
c
Aromaticity
ns p=1.00e+00
ns p=1.23e-02
ns p=1.60e-01
EpiGen
Natural
RandGen
Inference on PIRD
Extinction Coefficient
ns p=7.76e-01
ns p=1.84e-01
ns p=1.00e+00
Inference on PIRD
Instability Index
ns p=1.00e+00
ns p=1.00e+00
ns p=8.54e-01
Inference on PIRD
Isoelectric Point
ns p=8.45e-01
ns p=4.42e-01
ns p=1.00e+00
Inference on PIRD
Secondary Structure (Sheet)
** p=9.62e-03
ns p=6.53e-02
ns p=1.00e+00
Inference on PIRD
* p < 0.05
** p < 0.01
*** p < 0.001
d
Aromaticity
ns p=1.00e+00
*** p=5.95e-05
** p=1.69e-03
Inference on McPAS-TCR
Extinction Coefficient
** p=8.97e-03
*** p=3.03e-04
ns p=6.15e-01
Inference on McPAS-TCR
Instability Index
ns p=3.50e-01
ns p=1.90e-01
** p=2.28e-03
Inference on McPAS-TCR
Isoelectric Point
ns p=1.00e+00
* p=1.61e-02
* p=1.26e-02
Inference on McPAS-TCR
Secondary Structure (Sheet)
*** p=2.87e-07
* p=2.84e-02
* p=1.14e-02
Inference on McPAS-TCR
* p < 0.05
** p < 0.01
*** p < 0.001

Extended Data Fig. 4: **Chemical property distributions comparison. a–d.** Distribution of physicochemical properties across epitope sources, visualized using violin plots. Five properties are analyzed: Aromaticity, Extinction Coefficient, Instability Index, Isoelectric Point, and Secondary Structure (β-sheet content). Epitopes are categorized by source: EpiGen-generated (blue), naturally occurring in the test sets (red), and randomly generated (RandGen, red). The analysis spans four test sets: VDJdb (n=642), PIRD (n=545), IEDB (n=9,030), and McPAS-TCR (n=1,276), shown in panels **a**, **b**, **c**, and **d**, respectively. Violin plots incorporate box plots showing the median, interquartile range (IQR), and whiskers ($1.5 \times$ IQR). Statistical significance was determined using two-sided Mann-Whitney U tests with Bonferroni correction (*$p < 0.05$, **$p < 0.01$, ***$p < 0.001$, ns: not significant).

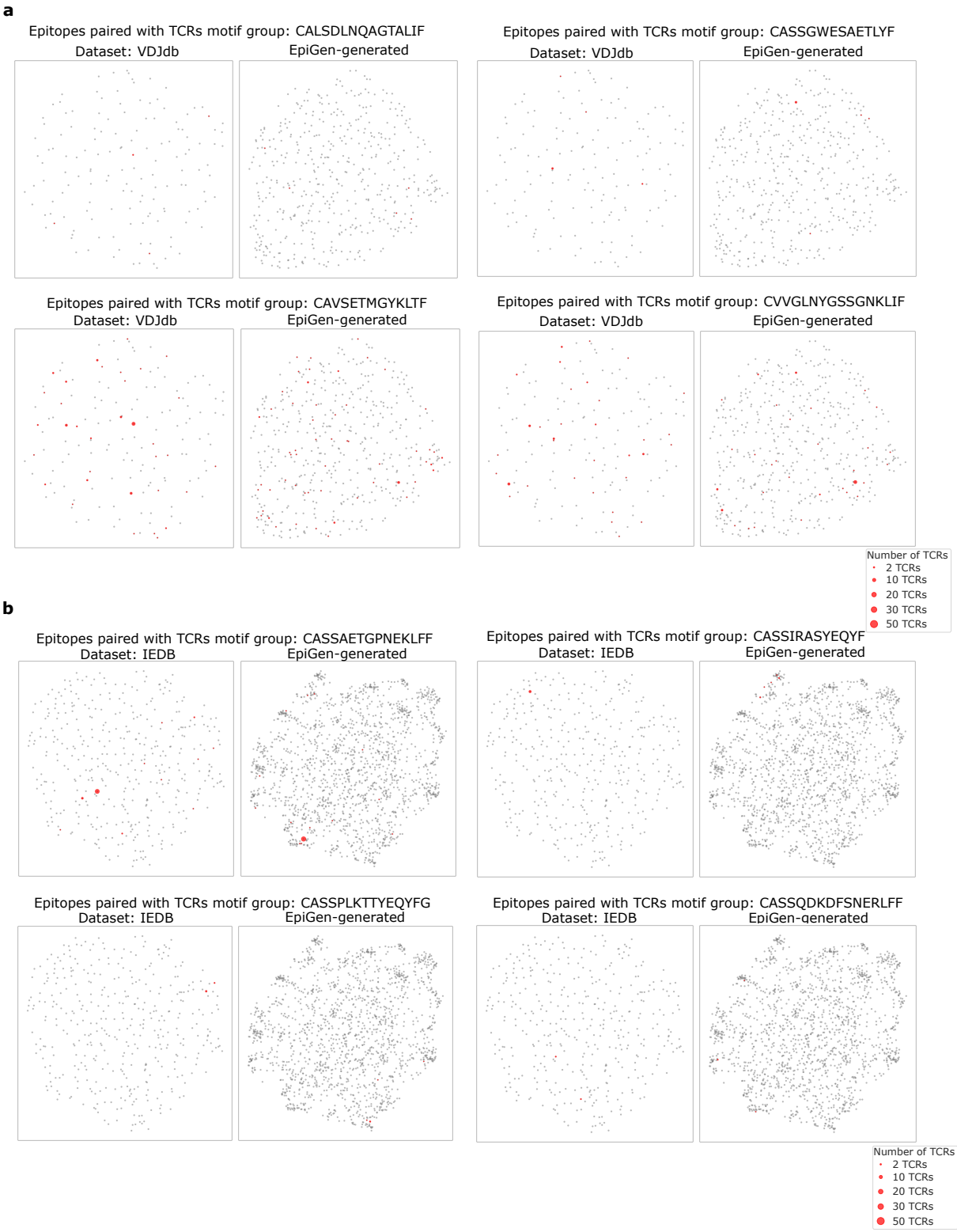
a
Epitopes paired with TCRs motif group: CALSDLNQAGTALIF
Dataset: VDJdb
EpiGen-generated
Epitopes paired with TCRs motif group: CASSGWESAETLYF
Dataset: VDJdb
EpiGen-generated
Epitopes paired with TCRs motif group: CAVSETMGYKLTF
Dataset: VDJdb
EpiGen-generated
Epitopes paired with TCRs motif group: CVVGLNYGSSGNKLIF
Dataset: VDJdb
EpiGen-generated
Number of TCRs
2 TCRs
10 TCRs
20 TCRs
30 TCRs
50 TCRs
b
Epitopes paired with TCRs motif group: CASSAETGPNEKLFF
Dataset: IEDB
EpiGen-generated
Epitopes paired with TCRs motif group: CASSIRASYEQYF
Dataset: IEDB
EpiGen-generated
Epitopes paired with TCRs motif group: CASSPLKTTYEQYFG
Dataset: IEDB
EpiGen-generated
Epitopes paired with TCRs motif group: CASSQDKDFSNERLFF
Dataset: IEDB
EpiGen-generated
Number of TCRs
2 TCRs
10 TCRs
20 TCRs
30 TCRs
50 TCRs

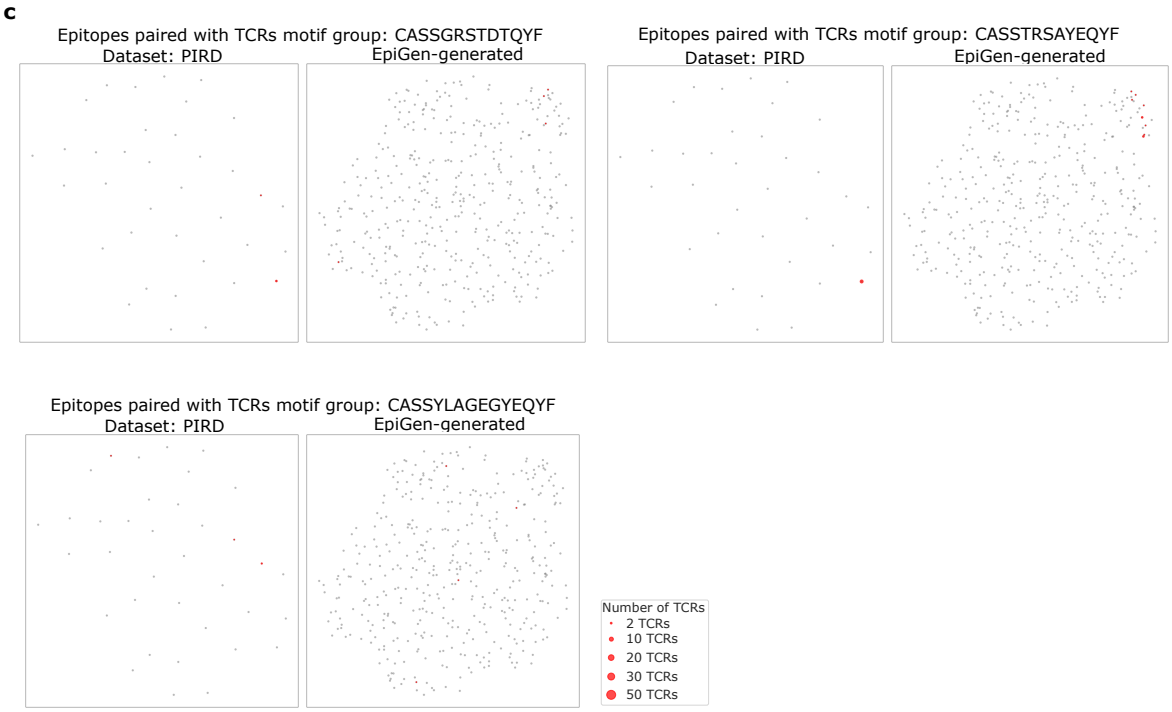
c
Epitopes paired with TCRs motif group: CASSGRSTDTQYF
Dataset: PIRD
EpiGen-generated
Epitopes paired with TCRs motif group: CASSTRSAYEQYF
Dataset: PIRD
EpiGen-generated
Epitopes paired with TCRs motif group: CASSYLAGEGYEQYF
Dataset: PIRD
EpiGen-generated
Number of TCRs
2 TCRs
10 TCRs
20 TCRs
30 TCRs
50 TCRs

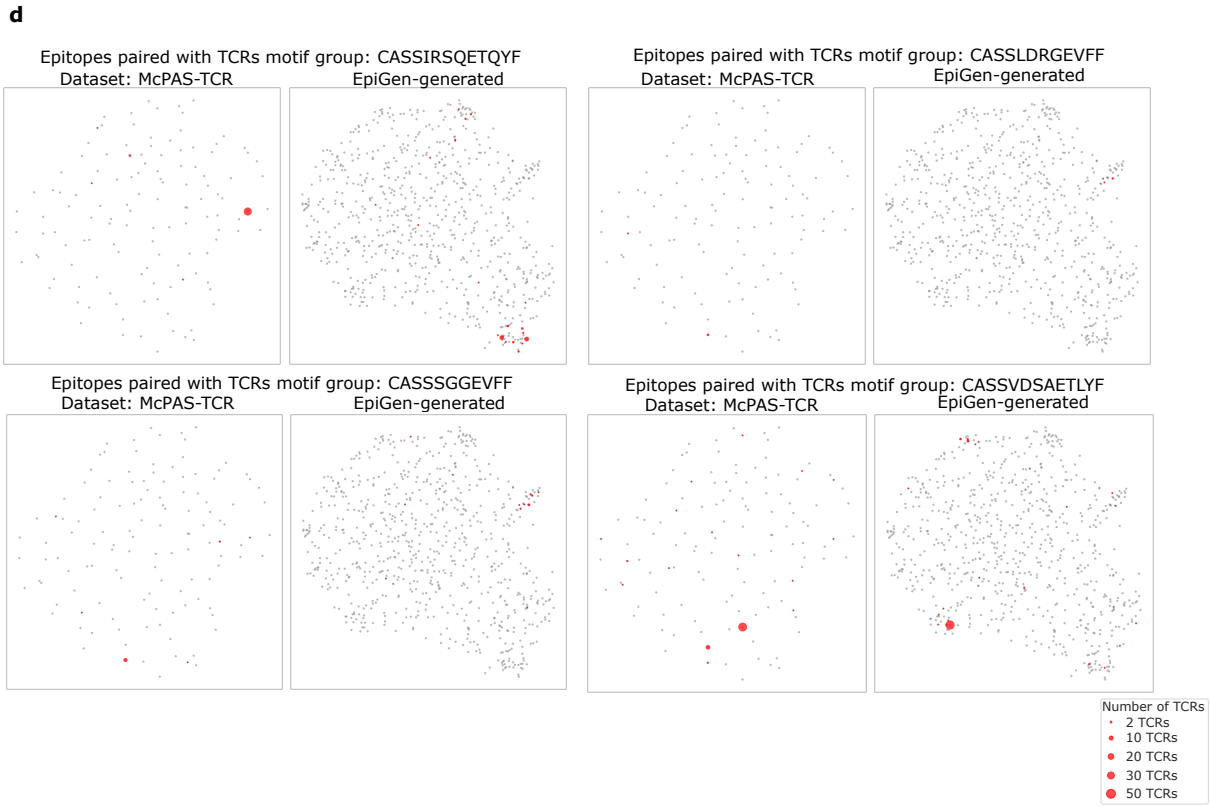
d
Epitopes paired with TCRs motif group: CASSIRSQETQYF
Dataset: McPAS-TCR
EpiGen-generated
Epitopes paired with TCRs motif group: CASSLDRGEVFF
Dataset: McPAS-TCR
EpiGen-generated
Epitopes paired with TCRs motif group: CASSSGGEVFF
Dataset: McPAS-TCR
EpiGen-generated
Epitopes paired with TCRs motif group: CASSVDSAETLYF
Dataset: McPAS-TCR
EpiGen-generated
Number of TCRs
2 TCRs
10 TCRs
20 TCRs
30 TCRs
50 TCRs

Extended Data Fig. 5: **Similar epitopes generated by EpiGen tend to be recognized by similar TCRs. a–d.** UMAP visualization of epitope sequence similarity spaces across four datasets: **a.** VDJdb, **b.** IEDB, **c.** PIRD, and **d.** McPAS-TCR. Sequence similarities were computed using the BLOSUM62 substitution matrix. Each point represents an epitope, with point size proportional to its paired TCR count. Epitopes recognized by TCRs sharing common motifs (identified by GLIPH2 analysis of test sets) are highlighted in distinct colors, while other epitopes are shown in grey. Three to four representative TCR motif groups are displayed per dataset. The visualization demonstrates both the broad distribution of generated epitopes and the clustering of similar epitopes recognized by TCRs with shared motifs.

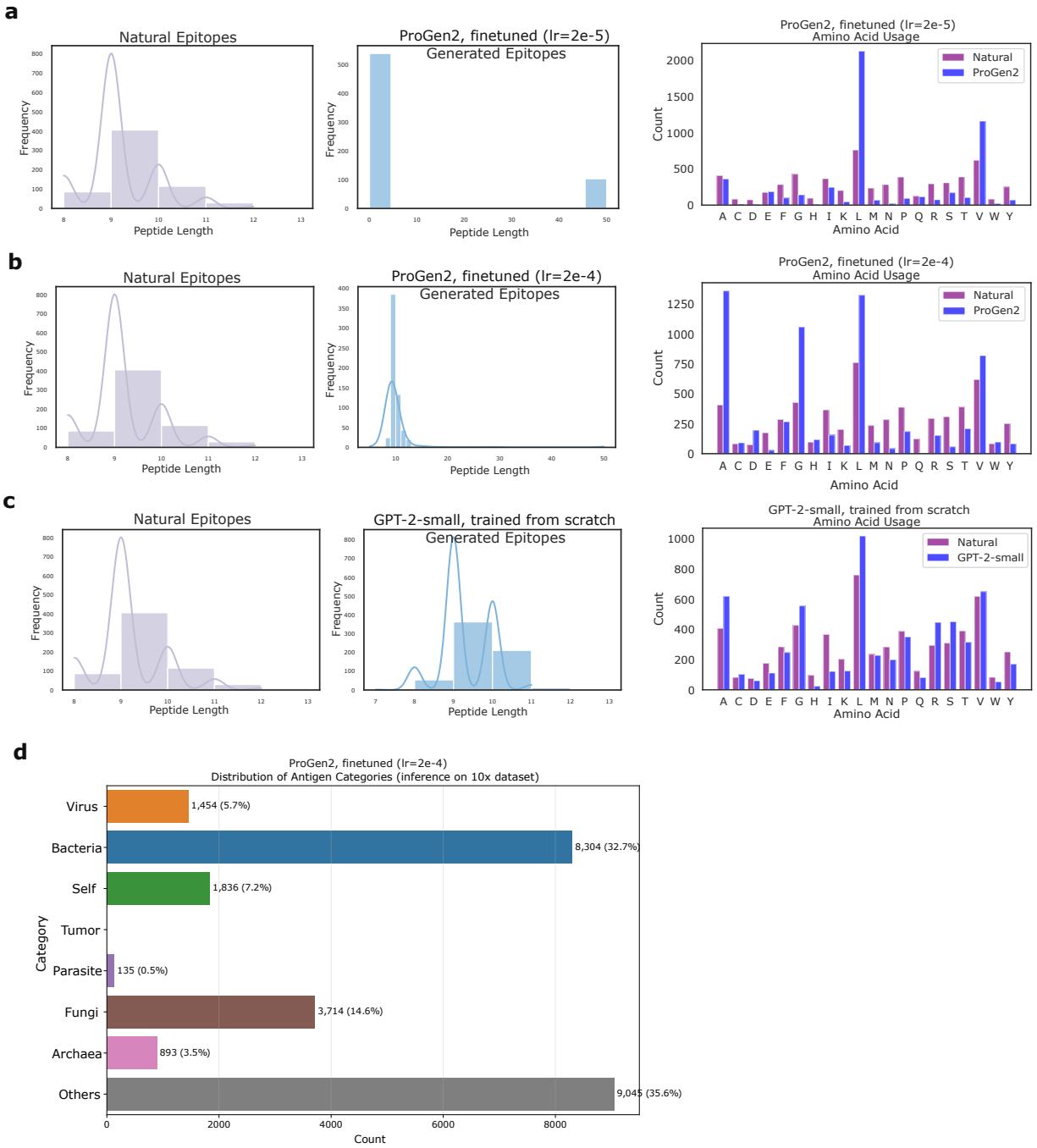

Extended Data Fig. 6: **Analysis of protein language model performance in epitope generation.** **a–c.** Comparative analysis of epitope length distributions between natural epitopes from the test set (left panels) and generated epitopes (middle panels) across three model configurations: **a.** ProGen2 fine-tuned with learning rate 2e-5, **b.** ProGen2 fine-tuned with learning rate 2e-4, and **c.** GPT-2-small trained from scratch with learning rate 2e-4, all using the publicly available training dataset. Right panels show amino acid frequency distributions comparing natural and generated epitopes for each model configuration. **d.** Distribution of predicted antigen categories from the 10x dataset using ProGen2 fine-tuned with learning rate 2e-4, demonstrating systematic biases in the model's predictions.

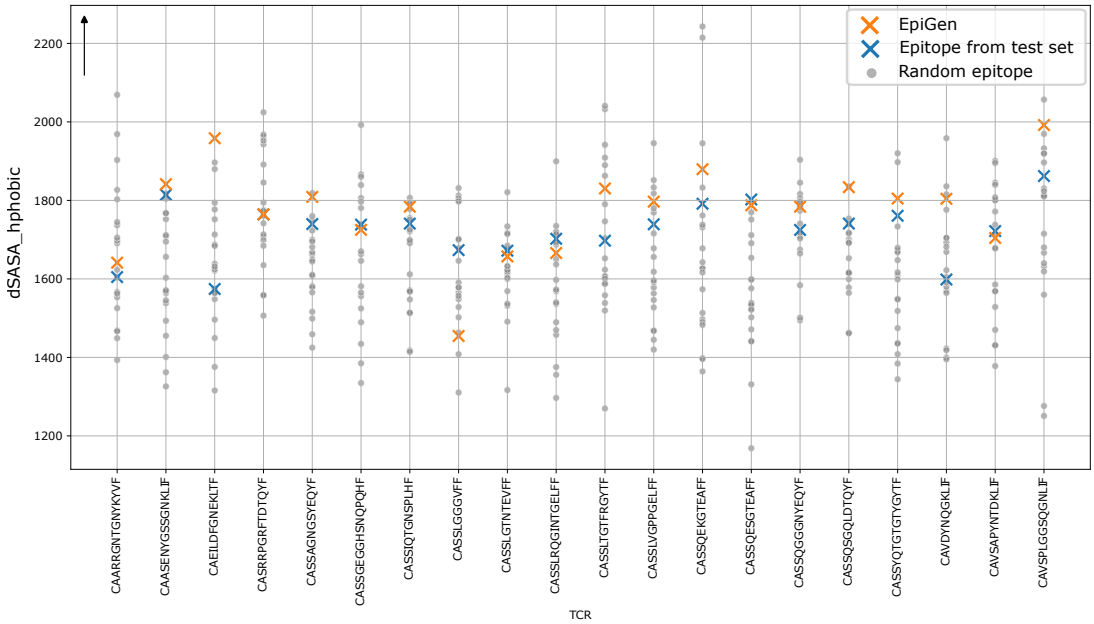

Extended Data Fig. 7: **Structural analysis using InterfaceAnalyzer with the generated epitopes.** Hydrophobic interaction analysis of TCR-pMHC complexes. Scatter plot showing dSASA_hphobic values (y-axis) for complexes containing EpiGen-generated epitopes (orange) or natural epitopes from the VDJdb test set (blue). Analysis conducted across 20 TCRs (x-axis), with 20 random epitopes per TCR serving as controls (grey). dSASA_hphobic measures the change in hydrophobic surface area that are hidden inside where dSASA stands for 'delta Solvent Accessible Surface Area'. Higher dSASA_hphobic values indicate higher structural stability. dSASA_hphobic was calculated using `Rosetta`'s `InterfaceAnalyzer`.

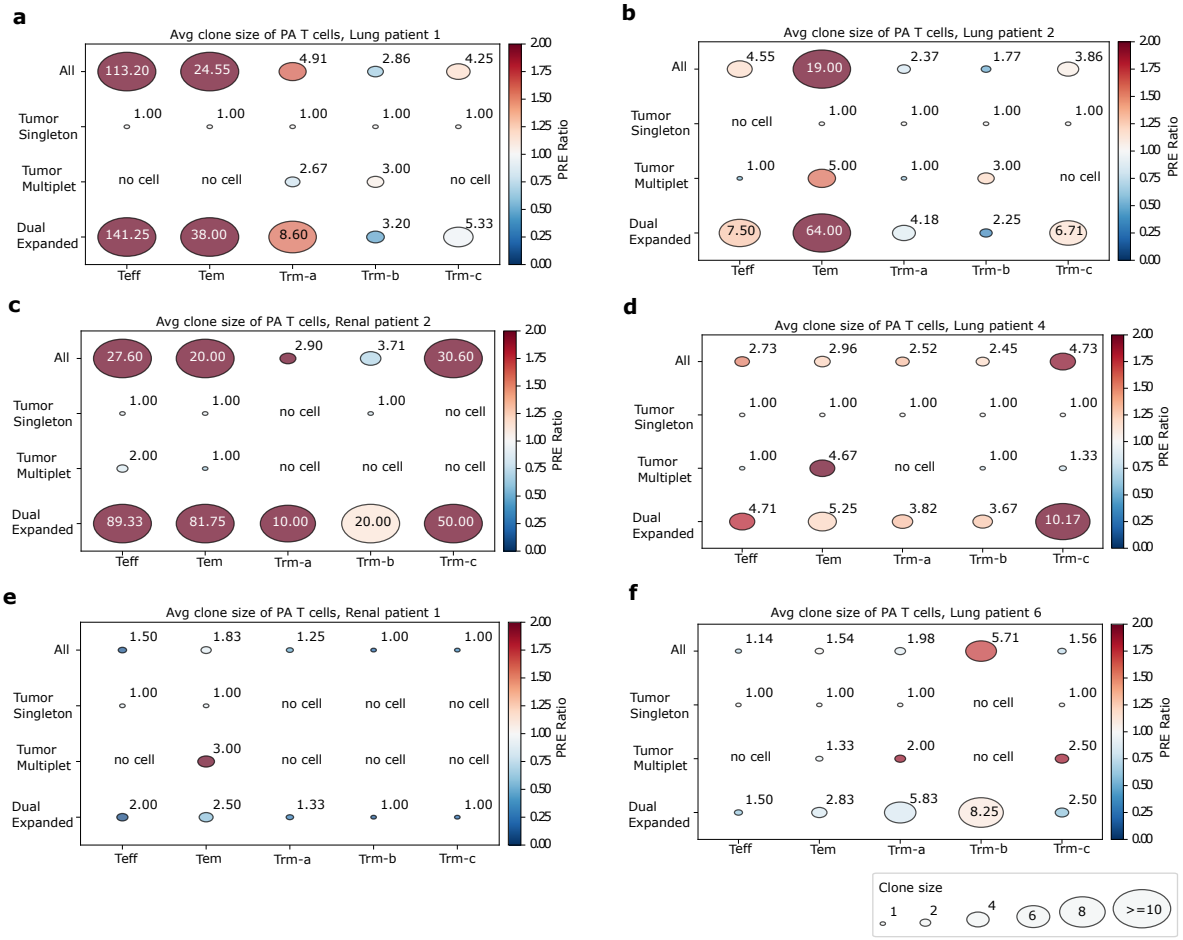

Extended Data Fig. 8: **Clonal expansion patterns of Phenotype-Associated T cells across patients. a-f.** Clonal expansion patterns across four site patterns (All, Tumor Singleton, Tumor Multiplet, and Dual Expanded) and five cell subtypes (Teff, Tem, Trm-a, Trm-b, and Trm-c) in six cancer patients (Lung 1, 2, 4, 6; Renal 1, 2). Color intensity indicates the Phenotype-Relative Expansion (PRE) ratio which means the mean clone size of PA T cells divided by that of NA T cells. Red indicates larger PRE ratio. Circle size represents mean clone size of PA T cells. Significant differences between clone sizes of PA and NA T cells were assessed using a one-sided Mann-Whitney U test, with p-values corrected for multiple testing via the Benjamini–Hochberg method. Only significant p-values are shown. "No cell" indicates absence of specific cell populations in that compartment. The plot highlights the heterogeneity of the clonal expansion patterns of PA T cells across patients.

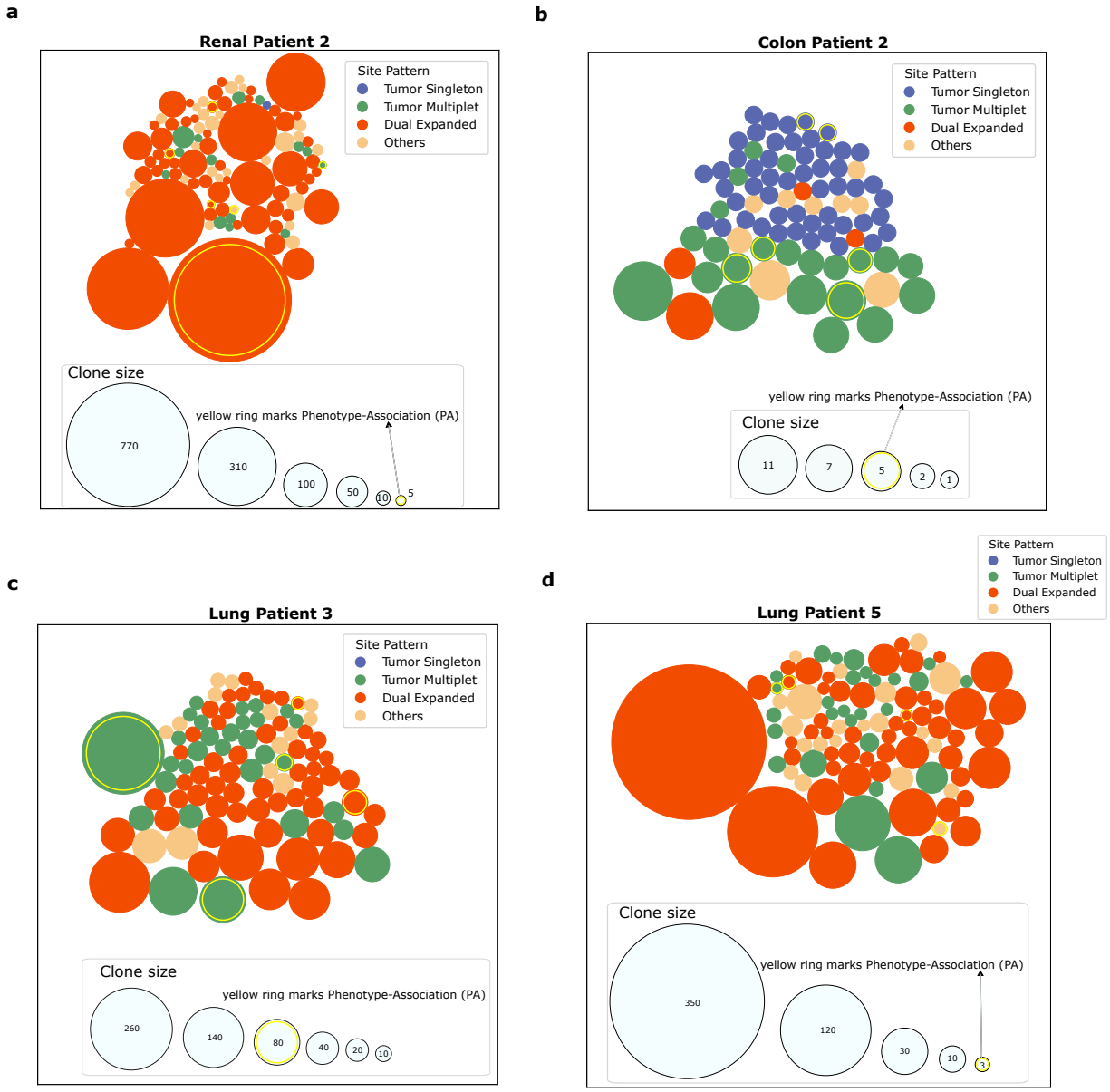

Extended Data Fig. 9: **Distribution of clonally expanded T cells in tumor and normal adjacent tissues. a-d.** Bubble plots illustrating the top 100 clonally expanded T cell clones in four patients: Lung patient 4, Lung patient 3, Endometrium patient 1, and Endometrium patient 3. Two site patterns are highlighted: Tumor Multiplet and Dual Expanded. Circle size represents clone size, while color denotes cell subtype. Phenotype-Associated (PA) T cells are marked by yellow rings. For Tumor Multiplet T cells, the Normal Adjacent Tissue (NAT) region is grayed out, indicating absence of these clones in that area. Dual Expanded T cells are present in both tumor and NAT regions.

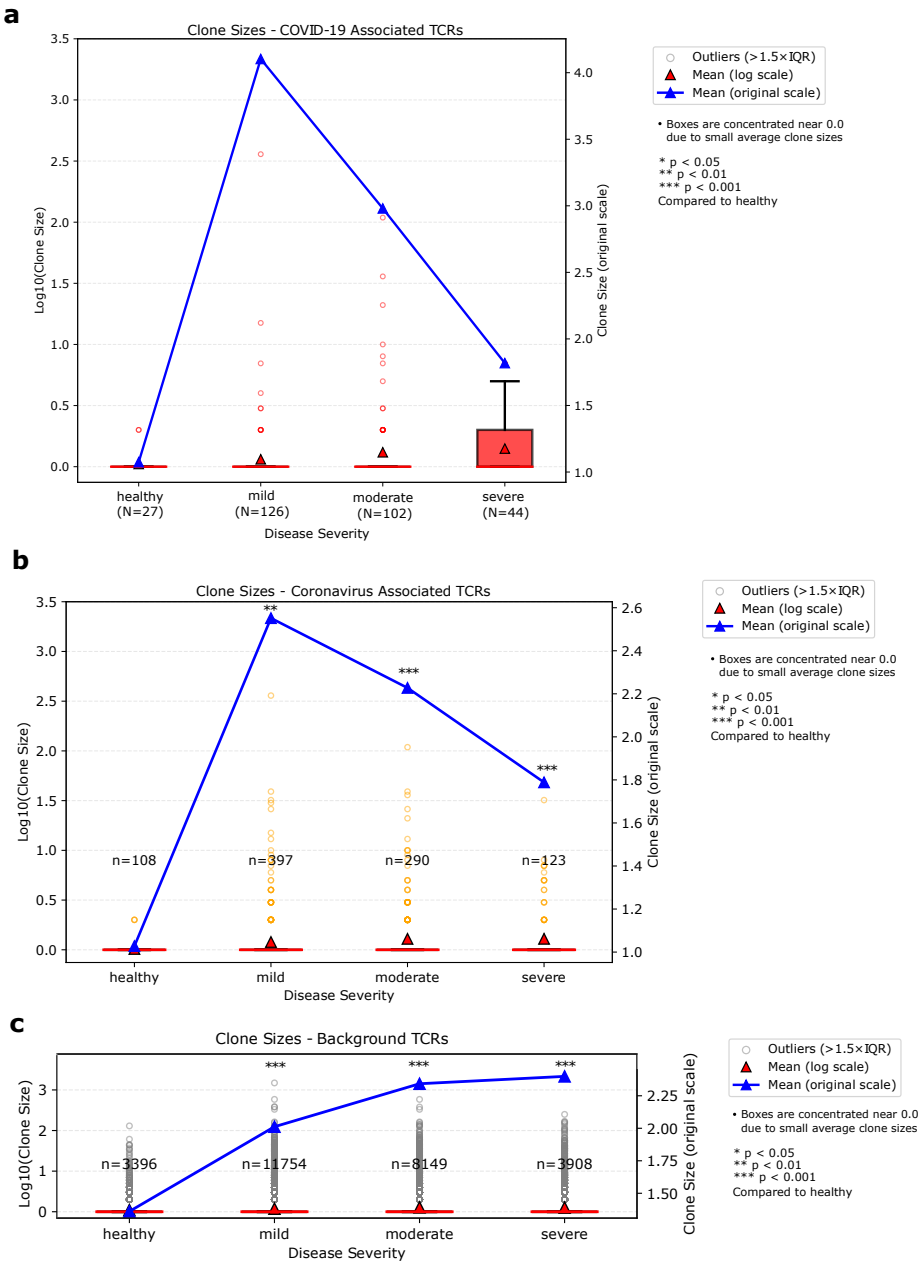

Extended Data Fig. 10: **Clonal expansion of COVID-19-Associated, coronavirus-associated, and background T cells by severity group.** **a-c.** T cell clonal expansion analysis across COVID-19 disease severity (healthy, mild, moderate, and severe) for three T cell categories: **a.** COVID-19-specific, **b.** broad coronavirus-associated, and **c.** non-COVID-19-associated T cells. T cells were labeled based on EpiGen-predicted epitopes followed by database querying to determine phenotype associations. Box plots display clone size distribution (left y-axis, log10 scale), with outliers (colored dots) representing significantly expanded clones. Mean clone sizes are indicated by red triangles (log scale, left y-axis) and blue triangles (original scale, right y-axis). Statistically significant differences compared to the healthy group were determined by one-sided Mann-Whitney U tests with p-values corrected using the Benjamini-Hochberg method.